

DTIC FILE COPY

2

AD-A219 651



WRDC-TR-89-2138

THREE-DIMENSIONAL ANALYSIS ON FLOW AND TEMPERATURE
DISTRIBUTIONS FOR AIRCRAFT FUEL THERMAL STABILITY

C. H. Oh
B. J. Merrill
R. P. Wadkins

IDAHO NATIONAL ENGINEERING LABORATORY
EG&G IDAHO, INC.
P. O. BOX 1625
IDAHO FALLS, ID 83415

JUNE 1989

INTERIM REPORT FOR THE PERIOD AUGUST 1988 - JUNE 1989

APPROVED FOR PUBLIC RELEASE; DISTRIBUTION IS UNLIMITED

AERO PROPULSION AND POWER LABORATORY
WRIGHT RESEARCH AND DEVELOPMENT CENTER
AIR FORCE SYSTEMS COMMAND
WRIGHT-PATTERSON AIR FORCE BASE, OHIO 45433-6563

DTIC
ELECTE
MAR 23 1990
E D

90 03 23 015

NOTICE

When Government drawings, specifications, or other data are used for any purpose other than in connection with a definitely Government-related procurement, the United States Government incurs no responsibility or any obligation whatsoever. The fact that the Government may have formulated or in any way supplied the said drawing, specifications, or other data, is not to be regarded by implication, otherwise in any manner construed, as licensing the holder, or any other person or corporation; or as conveying any rights or permission to manufacture, use, or sell any patented invention that may in any way be related thereto.

This report has been reviewed by the Office of Public Affairs (ASD/PS) and is releasable to the National Technical Information Service (NTIS). At NTIS, it will be available to the general public, including foreign nations.

This technical report has been reviewed and is approved for publication.



WILLIAM E. HARRISON III
Fuels Branch
Fuels and Lubrication Division



CHARLES L. DELANEY, Chief
Fuels Branch
Fuels and Lubrication Division

FOR THE COMMANDER



LEO S. HAROOTYAN, JR., Asst Chief
Fuels and Lubrication Division
Aero Propulsion and Power Laboratory

If your address has changed, if you wish to be removed from our mailing list, or if the addressee is no longer employed by your organization, please notify WRDC/POSF, Wright-Patterson AFB, Ohio 45433-6563 to help us maintain a current mailing list.

Copies of this report should not be returned unless return is required by security considerations, contractual obligations, or notice on a specific document.

UNCLASSIFIED

SECURITY CLASSIFICATION OF THIS PAGE

REPORT DOCUMENTATION PAGE				Form Approved OMB No 0704 0188	
1a REPORT SECURITY CLASSIFICATION Unclassified			1b RESTRICTIVE MARKINGS None		
2a SECURITY CLASSIFICATION AUTHORITY N/A			3 DISTRIBUTION/AVAILABILITY OF REPORT Approved for public release; distribution unlimited		
2b DECLASSIFICATION/DOWNGRADING SCHEDULE N/A					
4 PERFORMING ORGANIZATION REPORT NUMBER(S) N/A			5 MONITORING ORGANIZATION REPORT NUMBER(S) WRDC-TR-89-2138		
6a NAME OF PERFORMING ORGANIZATION EG&G Idaho		6b OFFICE SYMBOL (if applicable)	7a NAME OF MONITORING ORGANIZATION Wright Research & Development Center Aero Propulsion & Power Laboratory(WRDC/POSF)		
6c ADDRESS (City, State, and ZIP Code) P. O. Box 1625 MS 3515 Idaho Falls, ID 83415			7b ADDRESS (City, State, and ZIP Code) Wright-Patterson Air Force Base, Ohio 45433-6563		
8a NAME OF FUNDING/SPONSORING ORGANIZATION		8b OFFICE SYMBOL (if applicable)	9 PROCUREMENT INSTRUMENT IDENTIFICATION NUMBER FY1455-86-N0657		
8c ADDRESS (City, State, and ZIP Code)			10 SOURCE OF FUNDING NUMBERS		
			PROGRAM ELEMENT NO 63216F	PROJECT NO 2480	TASK NO 16
11 TITLE (Include Security Classification) Three-Dimensional Analysis on Flow and Temperature Distributions for Aircraft Fuel Thermal Stability					
12 PERSONAL AUTHOR(S) C. H. Oh, B. J. Merrill, and R. P. Wadkins					
13a TYPE OF REPORT Interim		13b TIME COVERED FROM Aug 88 TO June 89		14 DATE OF REPORT (Year, Month, Day) June 1989	
15 PAGE COUNT 68					
16 SUPPLEMENTARY NOTATION					
17 COSATI CODES			18. SUBJECT TERMS (Continue on reverse if necessary and identify by block number) Jet Fuel, Thermal Stability, JP-5, KIVA, Jet Fuel Thermal Oxidation Tester, JFTOT.		
FIELD	GROUP	SUB-GROUP			
21	21	07			
04	05	03			
19 ABSTRACT (Continue on reverse if necessary and identify by block number) This report presents flow and temperature distributions in the Jet Fuel Thermal Oxidation Tester (JFTOT), a device that has been used in thermal stability research of aircraft fuels. The Computational Fluid Dynamics and Chemistry (CFDC) model used in this study is based on the global Arrhenius type surface temperature-dependent correlation because of the lack of the existing experimental data. The initial attempt to calculate the deposit thickness and to simulate flow in the JFTOT is very encouraging.					
20 DISTRIBUTION/AVAILABILITY OF ABSTRACT <input checked="" type="checkbox"/> UNCLASSIFIED/UNLIMITED <input type="checkbox"/> SAME AS RPT <input type="checkbox"/> DTIC USERS			21 ABSTRACT SECURITY CLASSIFICATION Unclassified		
22a NAME OF RESPONSIBLE INDIVIDUAL William E. Harrison, III			22b TELEPHONE (Include Area Code) (513) 255-6601		22c OFFICE SYM. NO. WRDC/POSF

DISCLAIMER

This report was prepared as an account of work sponsored by the United States Government. Neither the United States nor any agency thereof, nor any of their employees, makes any warranty, expressed or implied, or assumes any legal liability or responsibility for the accuracy, completeness, or usefulness of any information, apparatus, product, or process disclosed, or represents that its use would not infringe privately owned rights. Reference herein to any specific commercial product, process or service by trade name, mark, manufacturer, or otherwise, does not necessarily constitute or imply its endorsement, recommendation, or favoring by the United States Government or any agency thereof. The views and opinions of the authors expressed herein do not necessarily state or reflect those of the United States Government of any agency thereof.

Accession For	
NTIS GRA&I	<input checked="" type="checkbox"/>
DTIC TAB	<input checked="" type="checkbox"/>
Unannounced	<input type="checkbox"/>
Justification	
By _____	
Distribution/	
Availability Code <input checked="" type="checkbox"/>	
Dist	Avail and/or Special
A-1	



SUMMARY

This report describes flow and temperature distributions in the Jet Fuel Thermal Oxidation Tester (JFTOT), a device that has been used in thermal stability research of aircraft fuels. A three-dimensional numerical analysis is presented in this report using the KIVA code. This work represents a preliminary attempt to "calibrate" a Computational Fluid Dynamics and Chemistry (CFDC) model using existing data from a fiber optics modified JFTOT.

Because of the limited amount of data on JFTOT experiments, the deposition model used in the study is the global type Arrhenius equation. Upon the finding of the parameters relevant to mass transfer, heat transfer, and fluid dynamics by future experiments, those relevant parameters can be combined altogether to define thermal instability of jet fuel with a higher degree of accuracy.

FOREWORD

This final report on the three-dimensional analysis of flow and temperature distributions for aircraft fuel thermal stability was prepared by the Core Design and Analysis Unit of EG&G Idaho, Idaho Falls, Idaho for the Aero Propulsion and Power Laboratory of Wright Research and Development Center, Air Force Systems Command, Wright-Patterson Air Force Base, Ohio. This project was funded through the Department of Energy (DOE) Pittsburgh Energy Technology Center during the period of August 1988 to June 1989. Dr. Nand K. Narain was the DOE-Pittsburgh Program Manager, Mr. William E. Harrison III was the Air Force Program Manager, and Dr. Chang H. Oh was the EG&G Program Manager.

TABLE OF CONTENTS

SECTION	TITLE	<u>Page</u>
I.	INTRODUCTION	1
II.	BACKGROUND	2
III.	DEPOSITION IN LITERATURE	3
IV.	JFTOT MODEL.	12
	1. Numerical Scheme and Modification	12
	2. Global Deposit Rate	16
	3. JFTOT Results on 3-D Analysis	19
	3.1 Sensitivity Study of Computational Grids	25
	3.2 Sensitivity Study of Computing Time.	35
	3.3 Deposit Calculation.	40
V.	CONCLUSIONS AND RECOMMENDATIONS FOR FUTURE STUDIES	45
VI.	REFERENCES	48
	APPENDIX A - DIMENSION TABLES FOR JFTOT MODEL.	A-1
	APPENDIX B - PROGRAM LISTING FOR DEPOSIT LAYER CALCULATION .	B-1
	APPENDIX C - ENLARGED FIGURES.	C-1

LIST OF FIGURES

<u>Figure</u>	<u>Page</u>
1. Cross Section of Corroded Aluminum.	4
2. Mass Transfer, Kinetics and Back Convection Model Proposed by Crittenden and Kolaczowski	9
3. Cross Section of FOM-JFTOT Heater Tube Holder	17
4. Overall Grid View of JFTOT Model of 8x24x24 Cells (Base Case)	20
5. Top View of JFTOT Model of 8x24x24 Cells.	21
6. Calculated Temperature Contours and Velocity Vectors at the Bottom, Mid-Height, and Top of the FOM-JFTOT (2600 cycles, time = 4.1 sec)	22
7. Calculated Radial Temperature and Velocity Distributions at the Bottom, Mid-Height, and Top of the FOM-JFTOT	24
8. The Axial Velocity Vectors Corresponding to the Azimuthal Slices of the Inlet	26
9. Overall Grid View of JFTOT Model of 8x24x14 Cells (Case 1).	27
10. Calculated Temperature Contours and Velocity Vectors at the Bottom, Mid-Height, and Top of the FOM-JFTOT (Case 1, 2600 cycles, time = 4.1 sec)	29
11. Calculated Radial Temperature and Velocity Distributions at the Bottom, Mid-Height, and Top of the FOM-JFTOT (Case 1).	30
12. The Axial Velocity Vectors Corresponding to the Azimuthal Slices of the Inlet and Exit Plane (Case 1)	31
13. Overall Grid View of JFTOT Model of 8x12x14 (Case 2).	32
14. Top View of JFTOT Model of 8x12x14 (Case 2)	33
15. Calculated Temperature Contours and Velocity Vectors at Bottom, Mid-Height, and Top of the FOM-JFTOT (Case 2, 2600 cycles, time = 4.1 sec).	34
16. Calculated Radial Temperature and Velocity Distributions at the Bottom, Mid-Height, and Top of the FOM-JFTOT (Case 2).	36
17. The Axial Velocity Vectors Corresponding to the Azimuthal Slices of the Inlet and Exit Plane (Case 2)	37

LIST OF FIGURES (continued)

<u>Figure</u>	<u>Page</u>
18. Calculated Velocity Vectors at the Mid-Height for Sensitivity Study (Base Case, 3650 cycles, time = 5.8 sec).	38
19. Calculated Velocity Vectors at the Mid-Height for Sensitivity Study (Base Case, 3950 cycles, time = 6.42 sec).	39
20. Calculated Temperature Contours at the Mid-Height for Sensitivity Study (Base Case, 3950 cycles, time = 5.8 sec).	41
21. Calculated Temperature Contours at the Mid-Height for Sensitivity Study (Base Case, 3950 cycles, time = 6.42 sec).	42
22. Calculated Deposit Thickness Profile on the FOM-JFTOT	44
C-1 Enlarged Velocity Vectors (Bottom) of Figure 6.	C-2
C-2 Enlarged Velocity Vectors (Mid-Height) of Figure 6.	C-3
C-3 Enlarged Velocity Vectors (Top) of Figure 6	C-4

LIST OF TABLES

<u>Table</u>	<u>Page</u>
1. Real-Time Deposition Data from Warner & Biddle.	18
A-1 Axial Dimension of 8x24x24 Cells.	A-1
A-2 Axial Dimension of 8x24x14 Cells.	A-2
A-3 Radial Dimension of JFTOT Model	A-2
A-4 Azimuthal Dimension of JFTOT Model.	A-3

SECTION I

INTRODUCTION

In order to improve understanding of the thermal stability of aircraft fuels that have been tested in the Fiber Optic Modified Jet Fuel Thermal Oxidation Tester (FOM-JFTOT)¹, a three-dimensional analysis on the FOM-JFTOT was performed. This level of flow detail was needed because of the FOM-JFTOT's unique configuration with the exit tube rotated 90° with respect to the flow inlet.

There are perhaps more computational fluid dynamics (CFD) codes²⁻⁵ that have the capability for three-dimensional analysis. All CFD codes use one of several methods to solve the governing Navier-Stokes equations. Each of these has its own merits and shortcomings. For this effort, the three-dimensional, time-dependent, finite difference KIVA⁶⁻⁸ code was selected and modified to analyze temperature and flow distributions of JP-5 fuel in the FOM-JFTOT owing to ease at which this code can be used to model different fluids flowing in arbitrary geometries.

Sections II and III discuss background and general deposition models shown in literature. Section II describes our JFTOT model and results from the study. Section V contains conclusions and recommendations for future studies.

SECTION II

BACKGROUND

Thermal stability of hydrocarbon fuels⁹⁻¹⁴ is expected to become increasingly important in the future. Especially, coal-derived jet fuels could be crucial to our national security if the supply of imported petroleum is disrupted. Speaking at the Spring National Meeting, John R. Rindt of the University of North Dakota Energy & Mineral Research Center noted that "domestic production currently supplies only 60% of our petroleum requirements." To take up the slack, synthetic fuels, such as those derived from coal, have grown increasingly appealing to the Department of Defense which, according to Rindt, "is the largest single consumer of liquid fuels in the United States." The by-products of coal gasification are a potential source for these jet fuels. Therefore, we expect that extensive research in this area will be undertaken to define and improve the thermal stability of existing jet fuels or the newly coal-derived jet fuels.

When jet fuels in an aircraft system are exposed to elevated temperatures, it causes higher thermal stresses, resulting in more thermal degradation. The thermal instability manifests itself as deposits on heat exchanger surfaces, fuel control valves and injector feed arms, leading to insufficient heat transfer and/or eventually mechanical problems. Many experimental studies⁹⁻¹⁴ have been performed in this area. No single report has undertaken a detailed coupled thermal fluids modeling effort, especially a 3-D analysis of flow and temperature distributions, for the JFTOT¹⁵ experiments. We hope this report will provide added insight into pertinent parameters that need to be treated self-consistently to obtain a useful computational fluid dynamics and chemistry (CFDC) model for future studies.

SECTION III

DEPOSITION IN LITERATURE

This section contains a literature survey¹⁶ on the fouling processes, chemical kinetic mechanisms and mathematical models of deposition. Fouling is a common phenomena occurring in many industrial processes: chemical¹⁷⁻²¹, petroleum²² aerospace²³⁻²⁴, nuclear²⁵, etc. Fouling that consists of the deposit of corrosion products or metal ions on the surface is classified into the corrosion fouling¹⁷, particulate fouling²⁶, precipitation fouling²⁷, chemical reaction fouling²⁸, etc. Corrosion fouling, for instance, can manifest itself in two ways. Corrosion can occur at the heat-transfer surface and the resulting corrosion products can form a deposit which will inhibit heat transfer. On the other hand, the deposit can be formed by corrosion products produced elsewhere in the system, which are then transported to the heat-transfer surface and deposited. This latter form of corrosion fouling is an occurrence of particulate fouling or of precipitation fouling. The processes associated with given categories of fouling appear to have been identified; however, in general, their exact character is uncertain.

In nuclear industries, fouling has been a critical issue to nuclear reactor safety.²⁵ Deposit of particulate metals and their oxides on the cladding material of the nuclear reactor is absolutely detrimental to reactor safety because it increases core temperatures because of low thermal conductivity and causes significant pressure drops in a narrow flow channel width, leading to fuel-plate instability. In order to overcome this problem in nuclear reactors, much research has been done to define the deposit mechanism and to predict the deposit thickness.

Figure 1 shows two layers of oxide deposited on the aluminum metal matrix that is being used as a cladding material attached to uranium oxide fuel. The deposition is basically a diffusion process. Depending on the interface temperature, aluminum oxide has a different number of water molecules, boehmite ($\text{Al}_2\text{O}_3 \cdot \text{H}_2\text{O}$) and bayerite ($\text{Al}_2\text{O}_3 \cdot 3\text{H}_2\text{O}$). In Figure 1, the boehmite layer, the inner layer on the surface, grows rapidly to the

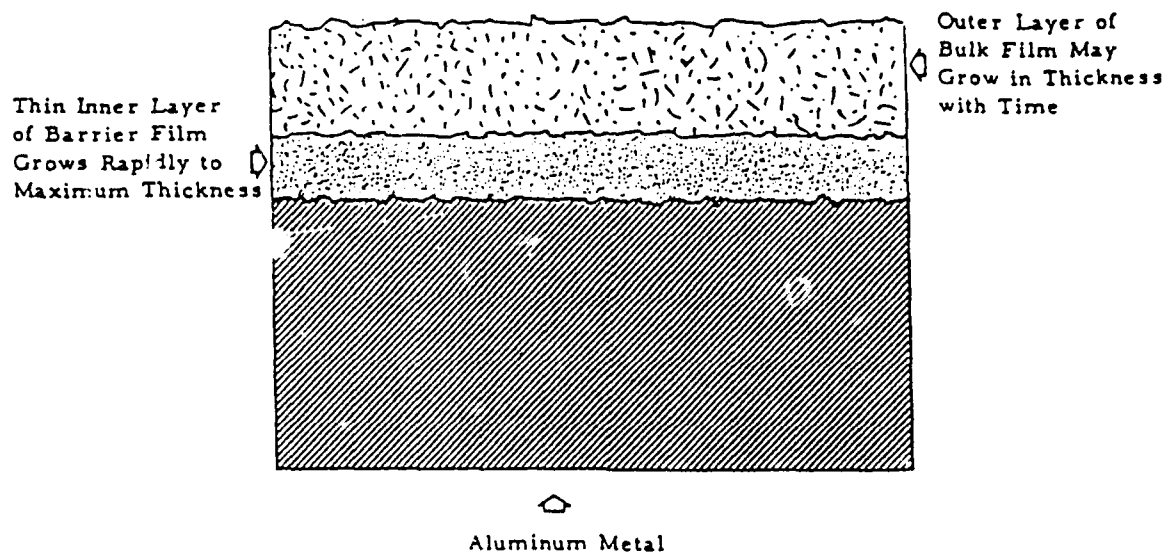


Figure 1. Cross Section of Corroded Aluminum.

maximum thickness while the outer layer, bayerite, grows in thickness with time, and as the flow velocity increases, the outer layer sloughs off. Griess et.al.²⁵ found that up to the point of film spallation about 70% of the oxidized aluminum remained on the surface as boehmite and the rest was lost to the water.

They developed an empirical deposit correlation considering only the data acquired with the water at a coolant pH of 5.0 and at heat fluxes between 3.15 and $6.3 \times 10^6 \text{ W/m}^2$:

$$X = c \theta^{0.778} \exp (-4600/T)$$

where X = oxide thickness, mils

c = 443 for pH 5, 1200 for pH 5.7 to 7, constant

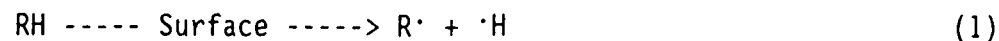
θ = exposure time, hours

T = absolute temperature, oxide-water interface, degrees Kelvin

The above Arrhenius type equation has been widely used to predict fouling deposits on the heated surface of nuclear reactors for more than two decades.

Regarding the chemical kinetics involved in deposition, autoxidation kinetic mechanisms of n-dodecane are well defined by many studies²⁹⁻³¹ to explain liquid phase oxidation of hydrocarbons by saturated oxygen. Basically, the autoxidation mechanism is as follows:

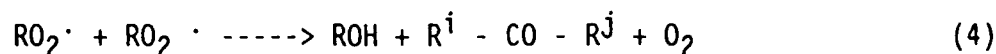
Initiation



Propagation



Termination



Initiation occurs on the hot heated surface by way of heterogeneous catalysis giving alkyl radicals in Reaction 1. These alkyl radicals react rapidly with molecular oxygen yielding secondary alkylperoxy radicals, RO_2^{\cdot} (Reaction 2). Alkylperoxy radicals, on the other hand, react much slowly with RH to form alkylhydroperoxides, ROOH shown in Reaction 3 which is usually the rate controlling propagation reaction. Of the three termination reactions, Reaction 4 appears to be the dominant process since alcohols and ketones are detected below 573 K. Reaction 5 and 6 are not important because of low concentration of R^{\cdot} . The autoxidation reaction occurs below 573 K. Especially, the hydroperoxide free radical in step 3 is fairly stable under 560 K. However, most experimental data, including Marteney and Spadaccini³², show the measurement of deposit even as low as 500 K. Also, some metal ion impurities such as sulfur, nitrogen, etc. apparently to have a significant effect on deposition. Taylor³³ carried

out deposit studies using six different jet fuels with different impurities and/or with deoxidation treatment. The results indicate that general trends are reduced deposit formations with deoxidized fuels. However, a deoxidized fuel with high concentration of total sulfur gave a reversed result, indicating oxygen is not the only element that causes deposition. Also, depending on the chemical structure of chemicals associated with sulfur atoms, sulfur may or may not act as an impurity. For instance, some structures of sulfur are inert even in the deactivation process of chemical catalysts. Also, the analysis of deposits indicates that the nature of deposits formed in a deoxygenated fuel is different from those formed in an air-saturated fuel, suggesting that such deposits are formed as a result of different classes of reactions. Therefore, detailed reactions leading to the formation of actual deposits need to be elucidated.

Deposition models are classified into reaction controlled deposition³⁴, diffusion controlled deposition³⁵, and a combination of deposition and removal³⁶ by shear forces or turbulent bursts.

The fouling process is a very complicated technical area. In order to model the fouling process completely, mass transfer, fluid dynamics, and chemical kinetics in models are required. Studying the deposition process for oil-rigs by using a sand-water slurry, Watkinson and Epstein²² developed an Arrhenius type correlation to determine the fouling rate. Using a momentum - mass-transfer analogy, the mass-transfer coefficient was related to fluid velocity. Also, assuming that sticking probability of particles on the surface is directly proportional to adhesive forces binding a particle to the wall, and that these adhesive forces depend on the surface temperature, they derived the following Arrhenius-type equation.

$$\dot{X} = \frac{A_1 (C_b - C_w) e^{-E/RT}}{U \sqrt{f}} - A_2 f U^2 X \quad (7)$$

where A_1 and A_2 are constants
 C is concentration of fouling species
 U is velocity
 f is Fanning's friction factor.

The constants A_1 and A_2 must be determined for a specific system and operating conditions. Also, one thing that should not be overlooked is that the Schmidt number must be unity in order to make a momentum-mass transfer analogy valid. Figure 2 contains an overall view of fouling process.³⁷ We believe that chemical reactions are taking place in the bulk stream and/or at the surface. Products generated from intermediate reactions in the bulk stream move toward the wall by diffusion.

Somewhere along the wall, the concentration of fouling products may become greater than that in bulk stream, leading to a back diffusion. Also, Figure 2 shows the deposit removal by fluid shear or turbulent bursts. Generally, diffusion on the surface is defined as follows:

$$N_p = K_p (C_{pb} - C_{pi})$$

or assuming the first-order chemical reaction on the surface

$$N_p = kC_{pi}$$

Crittenden and Kolaczowski³⁷ have extended the two-step mass transfer and kinetics model to include back diffusion. Thus,

$$\frac{dX_f}{dt} = \frac{1}{\rho_f} (N_p - N_f) \quad (8)$$

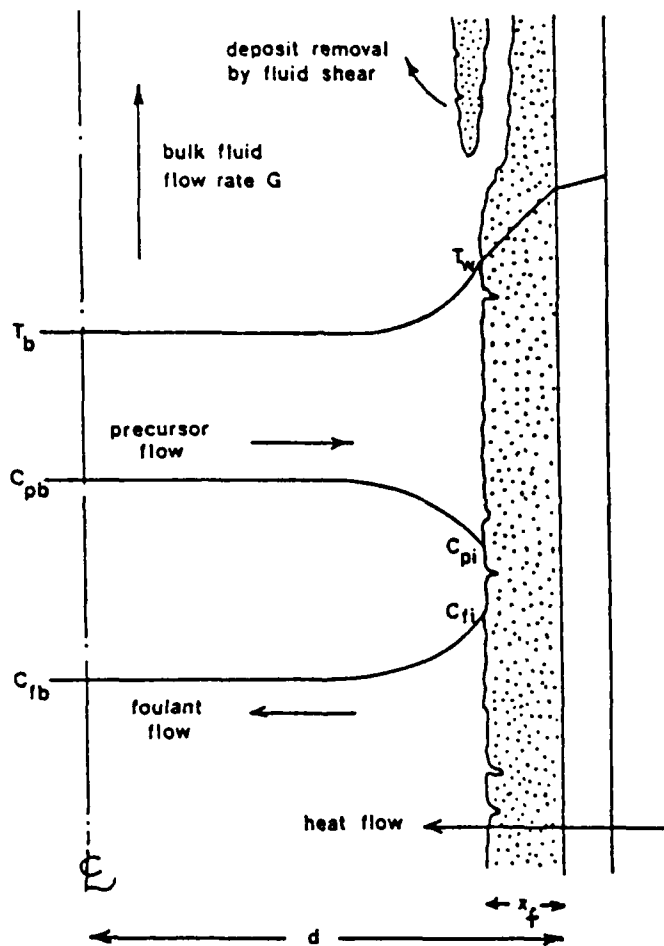


Figure 2. Mass Transfer, Kinetics and Back Convection Model Proposed by Crittenden and Kolaczowski.³⁷

where $N_f = K_f (C_{fi} - C_{fb})$

Assuming $C_{fi} \gg C_{fb}$ where back diffusion occurs, the overall fouling rate excluding removal by shear is

$$\frac{dR_f}{dt} = \frac{1}{\rho_f k_f} \left\{ \frac{C_{pb}}{\frac{1}{K_p} + \frac{1}{K}} - K_f C_{fi} \right\} \quad (9)$$

Replacing mass-transfer coefficients and reaction velocity constant by fluid velocities and the Arrhenius equation respectively gives the overall rate as follows:

$$\frac{dR_f}{dt} = \frac{1}{\rho_f k_f} \frac{C_{pb}}{\frac{\rho(d-2X_f)^{1.8} S_c^{0.67}}{0.67 \lambda \mu^{0.2} G^{0.8}} + \frac{1}{A \exp(-E/RT)}} - \frac{0.607 \lambda \mu^{0.2} G^{0.8} C_{fi}}{\rho(d-X_f)^{1.8} S_c^{0.67}} = \pi_1 \quad (10)$$

Equation 10 indicates that the fouling rate depends on the mass flow rate, G . Also, depending on the system and operating conditions, it can be either kinetics or diffusion controlled, leading to further simplifications of Equation (10). Including deposit removal by fluid shear, the overall rate can be written as

$$\frac{dR_f}{dt} = \pi_1 - \pi_2 R_f \quad (11)$$

assuming a first order dependence if deposit removal rate yields an asymptotic fouling resistance-time relationship with $R_f = 0$, when $t = 0$

$R_f = \pi_1 (1 - \exp(-\pi_2 t))$. Kern and Seaton³⁶ proposed that deposit removal can be assumed to be proportional to wall shear stress and deposit thickness:

$$\text{removal rate} = = \frac{\tau X_f}{\psi k_f} \quad (12)$$

where ψ is a function of deposit structure.

As described above, it appears that many deposition models are available in the literature. Parameters in those models are system dependent. No information appears in the literature about, for instance, quantitative concentration of hydroperoxides or oxygen in any jet fuels as a function of temperature. Therefore, this leads us to use a single correlation on which most experiments are based.

SECTION IV

JFTOT MODEL

1. NUMERICAL SCHEME AND MODIFICATION

Changes to the KIVA code were made to allow for the representation of fluids other than an ideal gas. These changes deal primarily with the implicit pressure convergence procedure of KIVA.² The partial differential equations solved in KIVA are the Navier-Stokes, conservation of mass, and internal energy equations. The solution procedure for these equations in KIVA combines the Implicit Continuous-fluid Eulerian (ICE)⁷ technique, with the grid rezoning of the Arbitrary Lagrangian-Eulerian (ALE)⁷ method. The implicitness of this method is the iterative updating of portions of mass, momentum, and internal energy conservation equations, while simultaneously requiring that the fluid pressure match that determined from a user supplied Equation of State (EOS).

KIVA solves the fluid equations in three phases. The first two, referred to as Phases A and B, constitute a Lagrangian calculation in which the computational grid is allowed to move with the fluid. During the third phase, (Phase C), the flow field variables are rezoned onto a new grid. Phase A is an explicit updating of various terms of the fluid equations. Phase B is the implicit update of the remaining terms of these equations. During Phase B, the following finite-difference approximations are used:

The Pressure Equation

$$P_{ijk}^B = P_{ijk}^A \left[1 - \gamma_{ijk}^A \left[\frac{V_{ijk}^B}{V_{ijk}^A} - 1 \right] \right] \quad (13)$$

The Volume Equation

$$V_{ijk}^B = V_{ijk}^A + \Delta t \sum_{\alpha} (uA)_{\alpha}^B \quad (14)$$

Equation for the Cell-faced Volume Fluxes

$$\begin{aligned} [\tilde{M}_{\alpha}^A + \tilde{S}_{\alpha}^A] [(uA)_{\alpha}^B - (uA)_{\alpha}^A] = & - \Delta t \sum_q \left[[1 - \phi_q] P_q^n + \phi_q P_q^B + \frac{2}{3} P_q^A A_q \right] \tilde{A}_q \cdot \underline{A}_{\alpha} \\ & + \Delta t [\tilde{M}_{\alpha}^A + \tilde{S}_{\alpha}^A] u_{\alpha}^n \cdot \frac{DA_{\alpha}}{Dt} \end{aligned} \quad (15)$$

Density Equation

$$[\rho_m]_{ijk}^B = [\rho_m]_{ijk}^A \frac{V_{ijk}^A}{V_{ijk}^B} \quad (16)$$

Internal Energy Equation

$$M_{ijk}^A [I_{ijk}^B - I_{ijk}^A] = - \frac{P_{ijk}^n + P_{ijk}^B}{2} [V_{ijk}^B - V_{ijk}^A] \quad (17)$$

The superscript of these equations refers to the value of that particular variable at the end of a given calculation phase, and the subscript refers to a given grid location. Some of the finite-difference approximations of Reference 2 have not been included in this list, since they do not enter into the present discussion.

In order to converge this set of equations, plus those not listed above, a volume residual is formed from Equation (14) as

$$[r_v]_{ijk} = V_{ijk}^B - \left[V_{ijk}^A + \Delta t \sum_{\alpha} (uA)_{\alpha}^B \right] \quad (18)$$

where the Phase B volume is derived from recasting Equation (13) in terms of cell pressure

$$V_{ijk}^B = V_{ijk}^A \left[1 + \frac{1}{\gamma_{ijk}^A} \left[1 - \frac{P_{ijk}^B}{P_{ijk}^A} \right] \right] \quad (19)$$

The pressure field of the computational grid is iteratively updated from Equations 15, 18, and 19 by the Conjugate Residual algorithm by utilizing the following change in cell volume residual with respect to cell pressure

$$\begin{aligned} \frac{\partial r_{ijk}}{\partial P_{ijk}} = & - \frac{V_{ijk}^A}{\gamma_{ijk}^A P_{ijk}^A} - \Delta t^2 \phi_{ijk} \frac{(3\bar{A}_R - \bar{A}_L) \cdot \bar{A}_R}{4(\bar{M}_R^A + \bar{S}_R^A)} + \frac{(3\bar{A}_L - \bar{A}_R) \cdot \bar{A}_L}{4(\bar{M}_L^A + \bar{S}_L^A)} + \frac{(3\bar{A}_T - \bar{A}_B) \cdot \bar{A}_T}{4(\bar{M}_T^A + \bar{S}_T^A)} \\ & + \frac{(3\bar{A}_B - \bar{A}_T) \cdot \bar{A}_B}{4(\bar{M}_B^A + \bar{S}_B^A)} + \frac{(3\bar{A}_F - \bar{A}_D) \cdot \bar{A}_F}{4(\bar{M}_F^A + \bar{S}_F^A)} + \frac{(3\bar{A}_D - \bar{A}_F) \cdot \bar{A}_D}{4(\bar{M}_D^A + \bar{S}_D^A)} \end{aligned} \quad (20)$$

By comparing Equation (20) with Equation (18), we see that the thermodynamic volume change, because of pressure for this iteration scheme, is as follows

$$\frac{\partial V_{ijk}^B}{\partial P_{ijk}^B} = - \frac{V_{ijk}^A}{\gamma_{ijk}^A P_{ijk}^A} \quad (21)$$

In order to include a fluid other than an ideal gas in this convergence scheme, we need only to define this quantity for the fluid of interest. For the present application, we have accomplished this by linearizing the EOS

$$d\rho = \left. \frac{\partial \rho}{\partial P} \right|_I dP + \left. \frac{\partial \rho}{\partial I} \right|_P dI \quad (22)$$

The thermodynamic volume change owing to pressure can be defined by differentiating the Density Equation, Equation (16), with respect to pressure.

$$\frac{\partial V_{ijk}}{\partial P_{ijk}} = - \frac{\rho_{ijk}^A V_{ijk}^A}{\rho_{ijk}^2} \frac{\partial \rho_{ijk}}{\partial P_{ijk}} = - \frac{\rho_{ijk}^A V_{ijk}^A}{\rho_{ijk}^2} \left[\frac{\partial \rho}{\partial P} \Big|_I + \frac{\partial \rho}{\partial I} \Big|_P \frac{\partial I}{\partial P} \right] \quad (23)$$

The change in internal energy with respect to pressure during this phase of the calculation can be obtained by differentiating Equation 17 with respect to pressure, with the added approximation that the average pressure of the P-V work term equals the old time value. The final result is that the following relationship for volume changes because of cell pressure

$$\frac{\partial V_{ijk}}{\partial P_{ijk}} = - \frac{\rho_{ijk}^A V_{ijk}^A}{\rho_{ijk}^2} \frac{\partial \rho}{\partial P} \Big|_I / \left[1 - \frac{P_{ijk}}{\rho_{ijk}^2} \frac{\partial \rho}{\partial I} \Big|_P \right] \quad (24)$$

The only remaining task is to define the EOS. For this application the following Stiffened EOS was adopted

$$P_{ijk} = a_s^2 (\rho_{ijk} - \rho_o) + (\gamma_{ijk} - 1) \rho_{ijk} I_{ijk} \quad (25)$$

$$\frac{\partial \rho}{\partial P} \Big|_I = \frac{1}{a_s^2 + (\gamma_{ijk} - 1) I_{ijk}} \quad (26)$$

$$\frac{\partial \rho}{\partial I} \Big|_P = \frac{\rho_{ijk} (\gamma_{ijk} - 1)}{a_s^2 + (\gamma_{ijk} - 1) I_{ijk}} \quad (27)$$

The convergence of these equations was tested for two extreme cases. The first was that of an ideal gas. The results were essentially identical to those of the original KIVA code. The second was in the limit as the fluid

compressibility, the square of the acoustic velocity of the stiffened EOS, approaches an infinite value (that is, an incompressible fluid). The results of this test indicate that as the velocity was increased, the velocity divergences of the grid cells approached zero, as would be expected for an incompressible fluid.

2. GLOBAL DEPOSIT RATE

The composition of deposits affords clues to the molecular species involved in deposit formation and the mechanism of formation. The chemical reaction mechanism of autoxidation that explains deposition can be found in the literature as mentioned earlier. However, there is no single datum that supports the quantitative effect of those chemical free radicals on deposition using JFTOT.

Since the majority of JFTOT experiments in the literature were not based on parameters involved in chemical reaction or mass transfer, a simple global type deposit rate that supports most JFTOT experiments was used in the preliminary calculation.

The experimental data set used in obtaining the Arrhenius factors was from Warner and Biddle.¹ They collected real-time deposition rate data using the Fiber Optic Modified JFTOT (FOM-JFTOT) shown in Figure 3.

Key features in the experiments include a means for producing quantitative data with the JFTOT, real-time data acquisition and display, and data at up to eight temperatures obtainable from one test. Table 1 is the typical data set of deposits that was built up to 0.14 microns. Based on Table 1, the Arrhenius factors were obtained using a linear regression analysis.

$$\text{deposit rate} = 155970 \exp (-19920/T(K)) \quad (28)$$

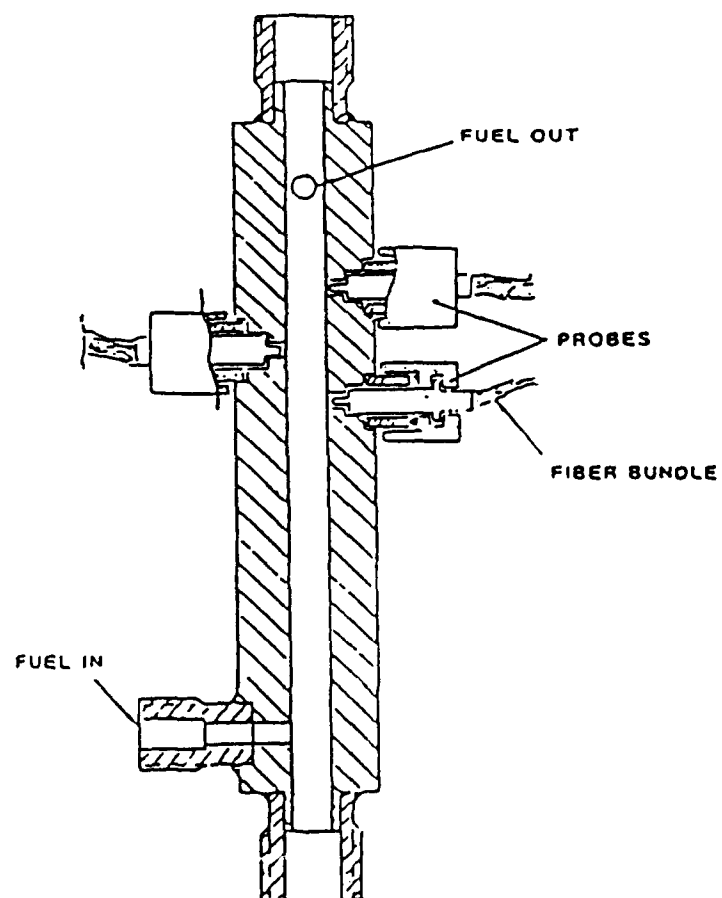


Figure 3. Cross Section of FOM-JFTOT Heater Tube Holder.

Table 1. Real-Time Deposition Data from Warner & Biddle

FF-3 JP-5 (470 B.P.) TEST DATA - ALL RUNS								
<u>TIME TO ACHIEVE 1ST MAX (0.14μ DEPOSIT)</u>								
<u>Test Temp (F)</u>	<u>Probe No.</u>	<u>Pos. (mm)</u>	<u>Tube Temp (F)</u>	<u>Minutes</u>				
				<u>Run No. 8</u>	<u>Run No. 9</u>	<u>Run No. 10</u>	<u>Run No. 11</u>	<u>Run No. 13</u>
550	1	28	522	107.5	100.0	92.5	--	106.0
	2	30	531	71.0	63.0	64.0	74.5	70.5
	3	32	538	61.5	52.0	--	53.5	58.5
	4	34	543	44.0	37.0	46.5	45.5	47.5
	5	36	550	38.0	32.5	37.5	40.5	38.5
				<u>Run No. 15</u>	<u>Run No. 16</u>			
500	1	28	475	--	--			
	2	30	482	--	--			
	3	32	489	245.0	240.0			
	4	34	495	203.0	--			
	5	39	500	171.0	156.0			
				<u>Run No. 27</u>	<u>Run No. 28</u>			
450	1	28	426	--	--			
	2	30	433	--	--			
	3	32	441	--	--			
	4	34	444	--	--			
	5	39	450	763.3	713.3			

3. JFTOT RESULTS ON 3-D ANALYSIS

Figure 4 shows the overall grid picture for the JFTOT model of 8 (radial) x 24 (azimuthal) x 24 (axial) cells. The detailed dimension of Figure 4 is in Table A-1. All the figures representing the JFTOT model in this report are not to exact scale. For instance, the radial and azimuthal dimension of JFTOT model were scaled up by a factor of 5 to provide a clear picture.

Figure 5 is the top view of 8 (radial)x24(azimuthal)x24(axial) cell model. In Figure 5, the azimuthal nodes of the inlet and outlet tubes to the JFTOT are $j=3$ through $j=7$ for inlet, and $j=9$ through $j=13$ for outlet. The 90° rotation and the cross-sectional area of the inlet and outlet tube were simulated to be identical to the JFTOT dimension ($4.901e-6 \text{ m}^2$, 5 azimuthal nodes, and 2 axial nodes in model).

The inner boundary is the heater surface of the JFTOT. The surface temperature distributions on the heater were obtained from Warner & Biddle's Table (550 F case). Since Warner & Biddle's experiments included only part of the test section (2.8 cm to 3.9 cm), the predicted temperature profile was correlated using a regression analysis. The following correlation was incorporated into KIVA.

$$T(K) = 519.6 - 3.676X + 0.2718X^2 - 0.003857X^3 \quad (29)$$

where X is axial length in mm.

The outer boundary temperature was taken as 300 K for the entire length of JFTOT. The inlet velocity to the JFTOT was set at 0.01 m/s.

Figure 6 (2600 cycles, time = 4.1 sec) shows the temperature contours and velocity vectors for the three azimuthal slices corresponding to the outlet plane, mid-height, and exit plane. The temperature contours show the penetration of thermal energy into the flow. At the inlet location,

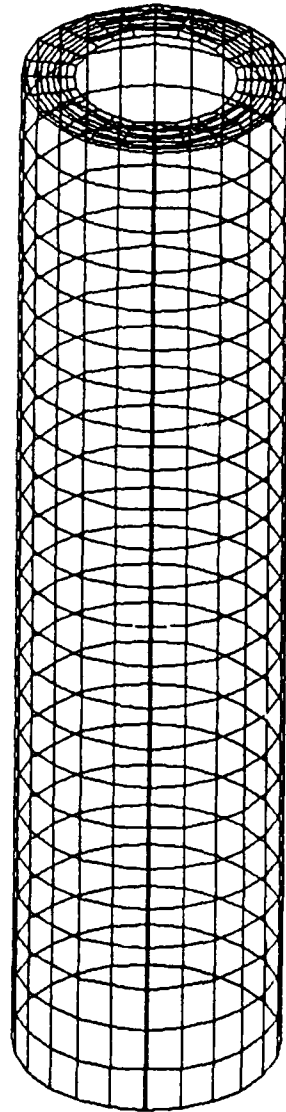


Figure 4. Overall Grid View of JFTOT Model of 8x24x24 Cells (Base Case).

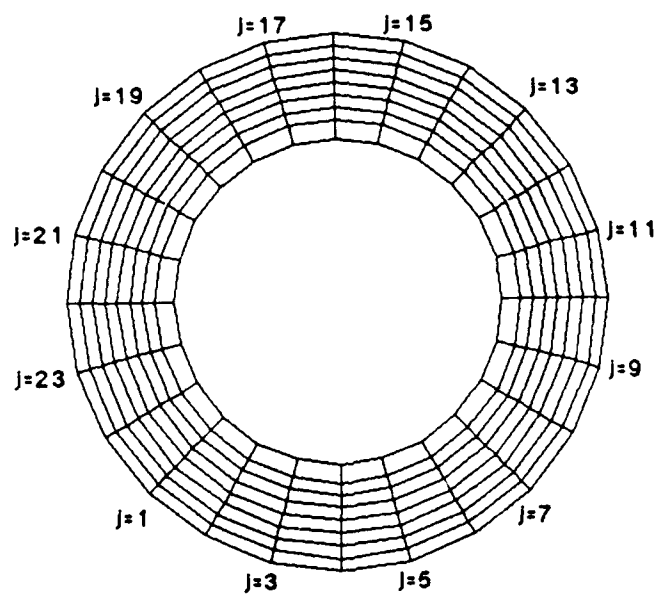


Figure 5. Top View of JFTOT Model of 8x24x24 Cells.

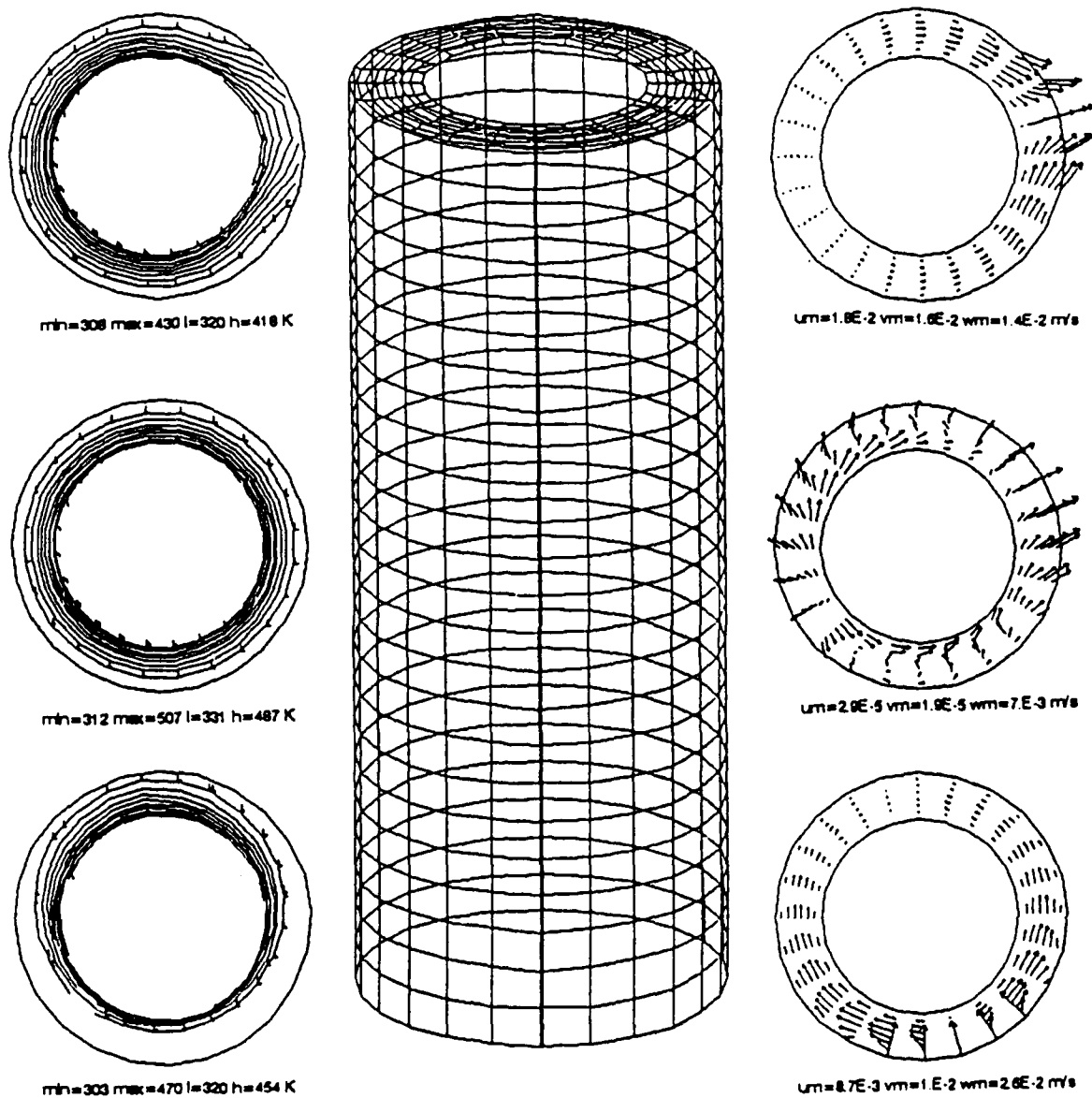


Figure 6. Calculated Temperature Contours and Velocity Vectors at the Bottom, Mid-Height, and Top of the FOM-JFTOT (2600 Cycles, Time = 4.1 Sec).

the temperature contours are closely spaced in the vicinity of the heater tube surface on the side of the tube closest to the inlet. On the opposite side of the tube the contours are more widely spread.

This indicates that thermal energy is penetrating into the fuel much further on the back side of the tube, where radial and azimuthal velocities are nearly stagnant. At the mid-height location, contours are almost evenly spaced, while the velocity vectors appear to be outward. However, since vectors are originated inside the computing grid domains, this indicates the instantaneous direction of the local flow. A better picture can be seen in the Appendix. The maximum axial and azimuthal velocity indexed as u_m and v_m , respectively, are much smaller than that of axial velocity (w_m) by more than a factor of 200.

As we move to the azimuthal plane at the exit, smaller temperature gradients are apparent on the side corresponding to the flow exit, while in the other region, velocity contours are nearly symmetric. The magnitude of the velocity vectors are not relatively comparable from one plane to the others.

KIVA calculates fluid temperatures corresponding to each computational cells from minimum to maximum indexed as min and max, respectively in Figure 6. However, temperature contours only between l (low) and h (high) are plotted in this figure.

Figure 7 shows the radial profiles of temperature and velocity at the same axial plane as Figure 6 for the azimuthal location corresponding to the exit. The velocity profiles at the entrance and mid-height are basically parabolic, indicating a simple pipe flow, whereas at the exit the axial velocity at the outer boundary indicates the presence of the outlet pipe. The axial, radial, and azimuthal velocities at the exit are nearly in the same order of magnitude as shown in Figure 6. At the inlet plane, the temperature gradients appear steeper than those of mid-height, and exit. A steep temperature gradient near the tube surface is equivalent to the dense contours shown in Figure 6. At the mid-height the temperature

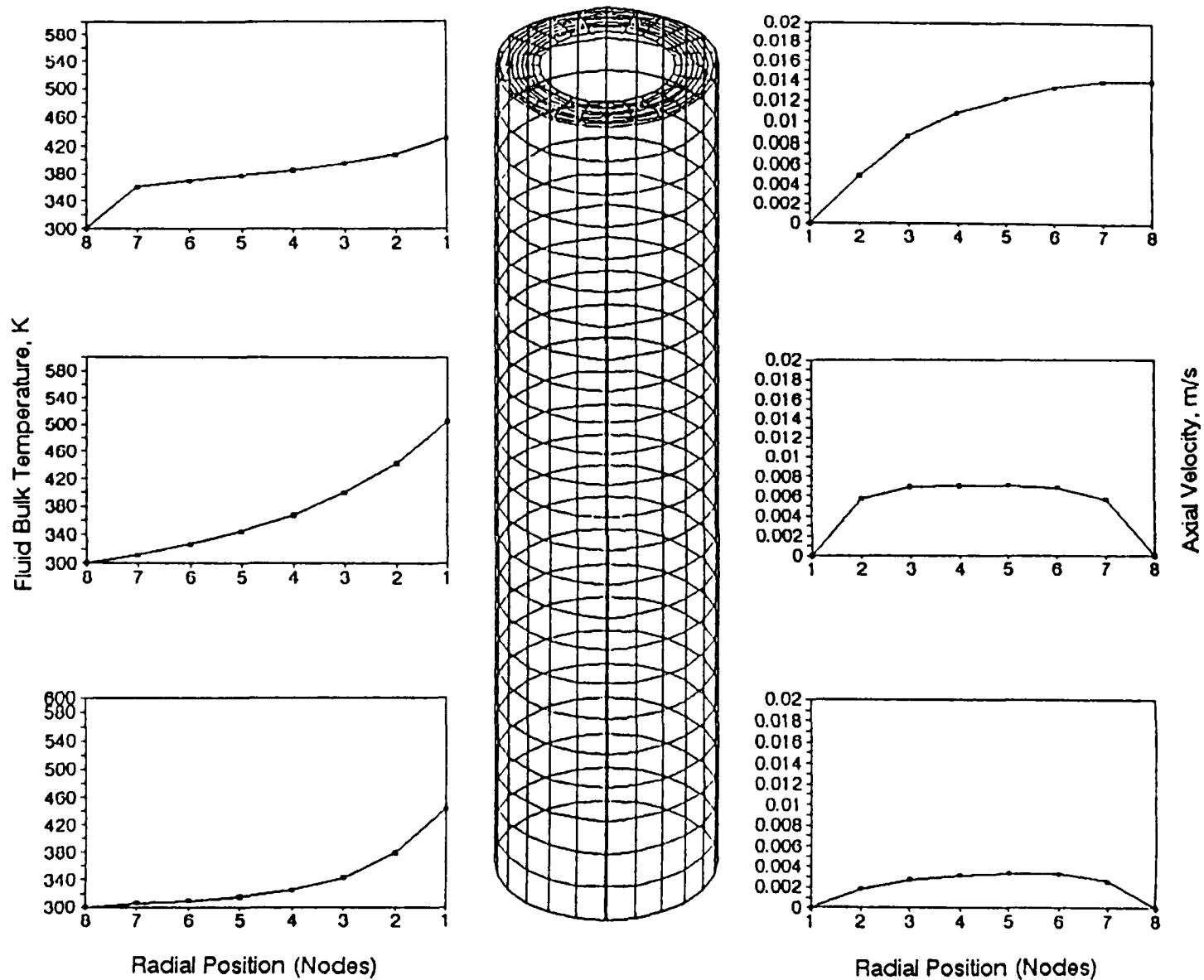


Figure 7. Calculated Radial Temperature and Velocity Distributions at the Bottom, Mid-Height, and Top of the FOM-JFTOT.

gradient is still steep, but not as steep as it was at the inlet plane. This again corresponds to the spreading of the temperature contour shown in Figure 6. At the exit plane, the temperature gradient is not significantly large across the tube radius, indicating that the thermal energy has penetrated the flow channel gap.

An added view of the flow is presented in Figure 8, which shows the entire axial velocity vectors corresponding to the azimuthal slice of inlet and exit planes, respectively.

At the inlet plane, the velocity vectors on the opposite side of the inlet stagnate. At the mid-height, the velocity vectors appear symmetric. The complex radial and azimuthal mid-plane flow pattern shown in Figure 6 was not significant to these calculations because their magnitudes are much smaller than those of Figure 8. At the exit, vectors on the opposite side of the exit appear small as would be expected.

3.1 Sensitivity Study of Computational Grids

The following two cases were examined to find a sensitivity of added or reduced computational nodes on the predicted temperature and velocity distributions described in the preceding section, hereafter called the Base Case.

The computational cells or elements of Case 1 consist of 8(radial)x 24(azimuthal)x14(axial), which is a reduced number of cells in the axial coordinate from that of the Base Case. All cases for the sensitivity studies were run up to 2600 cycles, time = 4.1 seconds.

Figure 9 shows the overall grid for Case 1. Again, the dimension of the radial and azimuthal coordinates was scaled by a factor of 5. In order to have the same cross-sectional area of the inlet and the outlet tube as that of the base case ($4.91 \text{ e-}6 \text{ m}^2$), the height of the inlet and outlet tube remained the same as that of the base case. The detailed dimension of the computational grids is given in the Appendix.

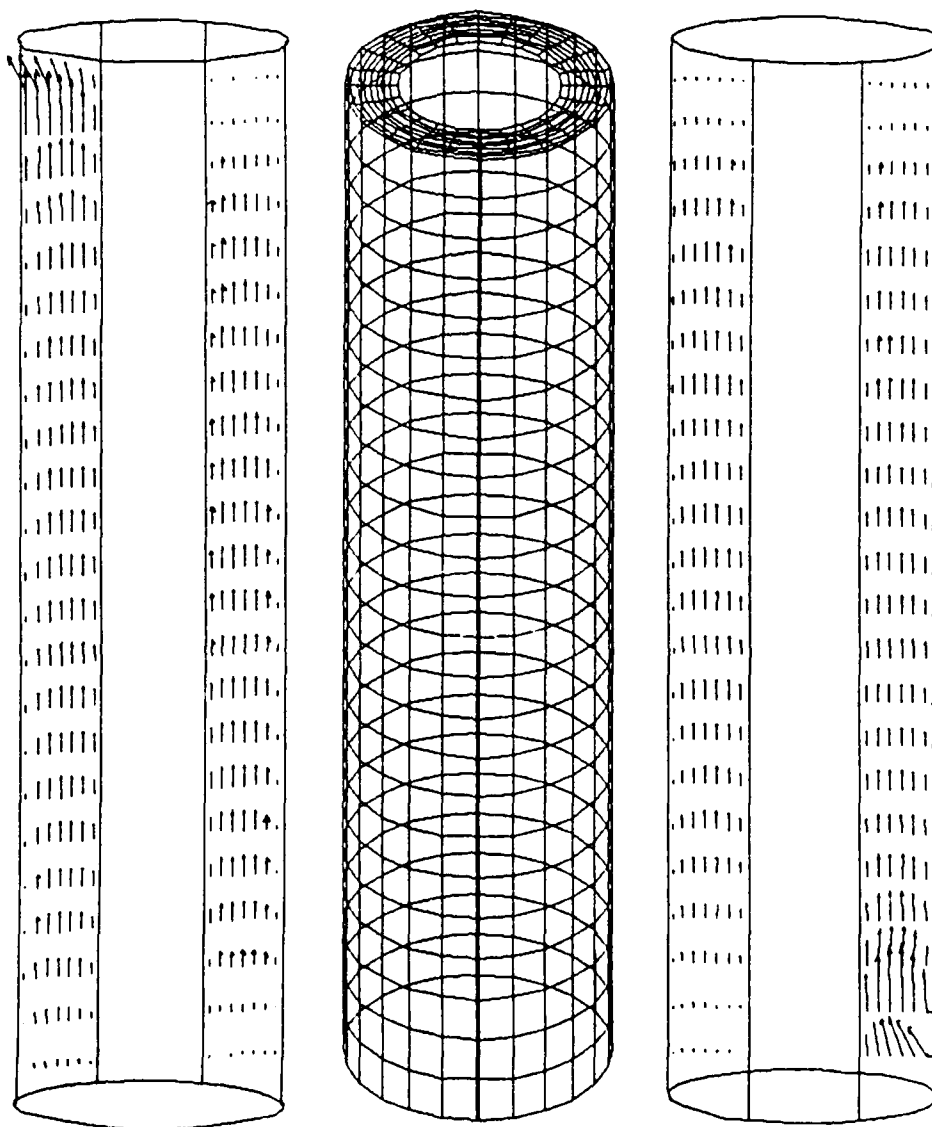


Figure 8. The Axial Velocity Vectors Corresponding to the Azimuthal Slices of the Inlet.

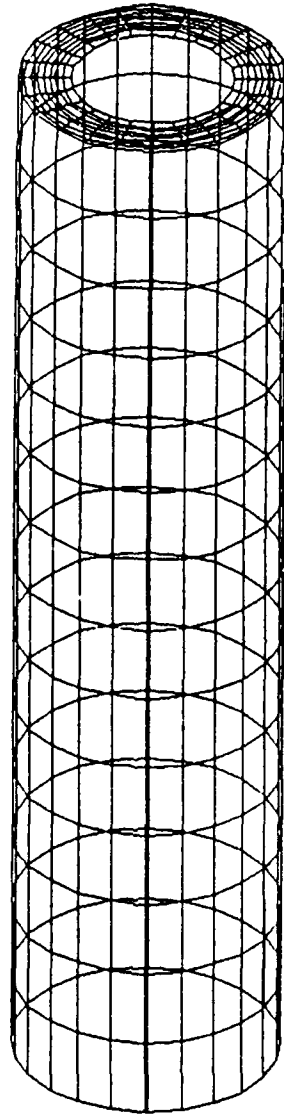


Figure 9. Overall Grid View of JFTOT Model of 8x24x14 Cells (Case 1).

Figure 10 is equivalent to Figure 6. The temperature contour pattern appears nearly the same as those in Figure 6. Since the surface temperature correlation (eq. 29) is a parabolic profile, the less accurate axial description resulted in a lower fluid exit temperature. The velocity vectors at the mid-height appear inward especially on the side corresponding to the inlet tube, while the velocity vectors in Figure 6 are more dispersed at the mid-point. This indicates that with more computational cells in the axial coordinates, radial and azimuthal flow patterns appear more dispersed. However, the fairly insignificant magnitude of the radial and azimuthal velocity compared to that of the axial velocity does not change the thermal equilibrium.

Figure 11 contains the radial temperature and axial velocity profiles at three axial locations, equivalent to those of Figure 7. No differences are noted between those two figures.

Figure 12 shows the entire axial velocity vector profile azimuthally sliced at the location corresponding to the inlet and outlet tube, which can be compared to Figure 8. Some vectors at the mid-height shown in Figure 12 show inward flow pattern as also shown in Figure 10. However, as mentioned earlier, the magnitude of the radial and azimuthal velocity vectors is much smaller compared to those of axial velocity to affect the thermal energy distribution in JFTOT.

The computational cells of Case 2 shown in Figures 13 and 14 consist of 8(radial)x12(azimuthal)x14(axial) cells, which is a reduction in the number of cells in the azimuthal direction compared to Case 1. Again, the cross-sectional area of the computational cells was identical to the size of inlet and outlet tubes of FOM-JFTOT. Figure 15 shows the obtained temperature contours and velocity vectors azimuthally sliced at the inlet, mid-height, and exit. These slices compare with Figures 6 and 10 for the Base Case and Case 1, respectively.

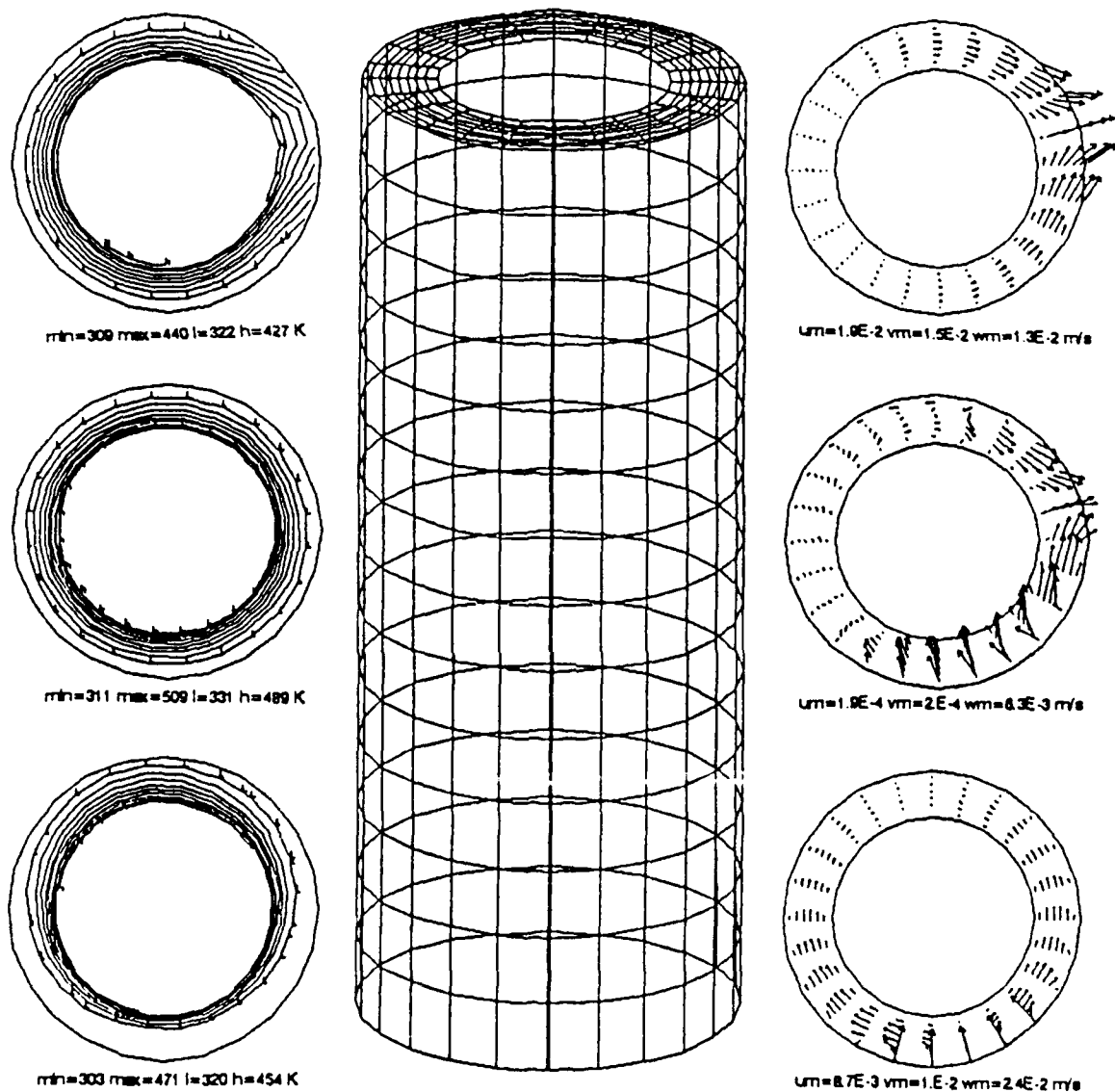


Figure 10. Calculated Temperature Contours and Velocity Vectors at the Bottom, Mid-Height, and Top of the FOM-JFTOT (Case 1, 2600 Cycles, Time = 4.1 Sec).

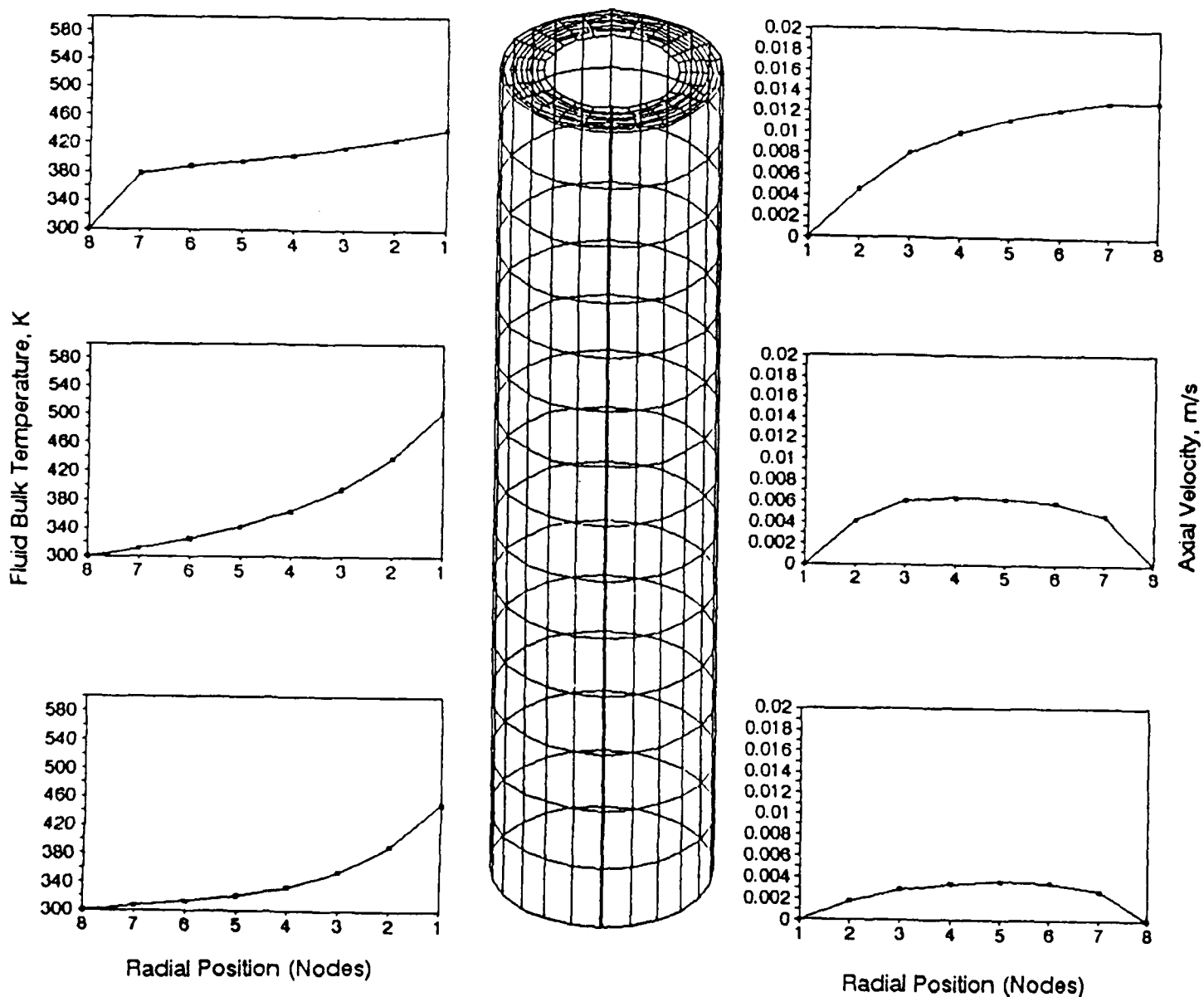


Figure 11. Calculated Radial Temperature and Velocity Distributions at the Bottom, Mid-Height, and Top of the FOM-JFTOT (Case 1).

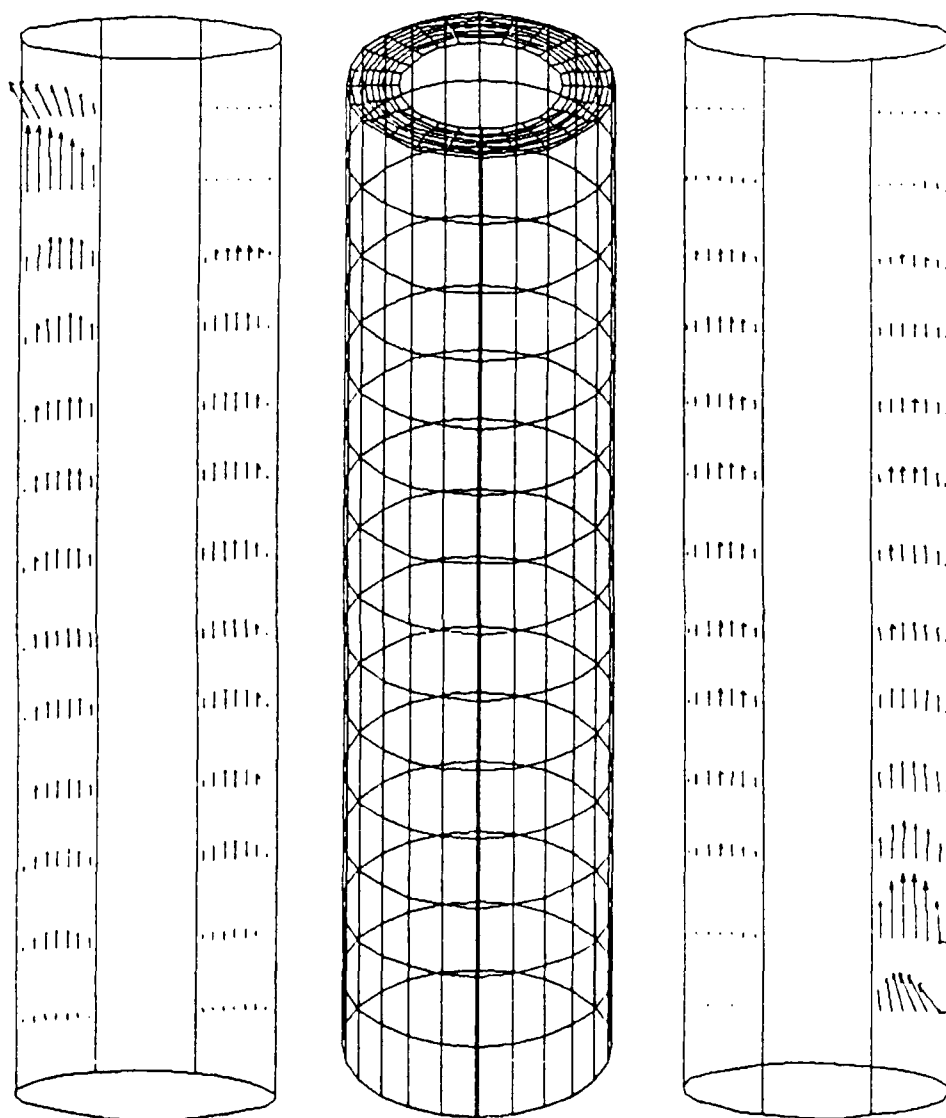


Figure 12. The Axial Velocity Vectors Corresponding to the Azimuthal Slices of the Inlet and Exit Plane (Case 1).

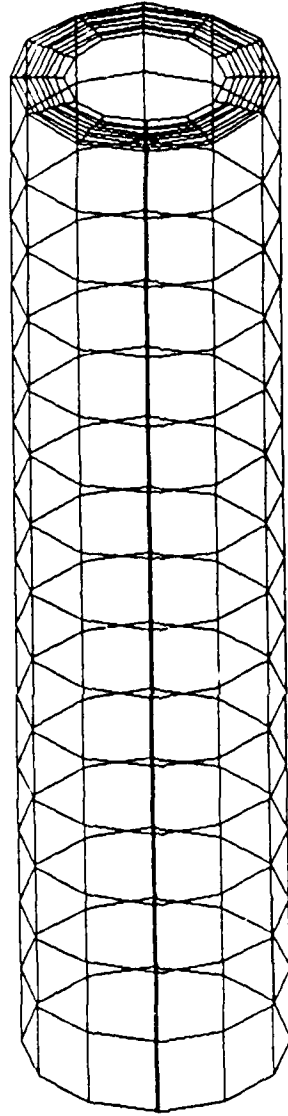


Figure 13. Overall Grid View of JFTOT Model of 8x12x14 (Case 2).

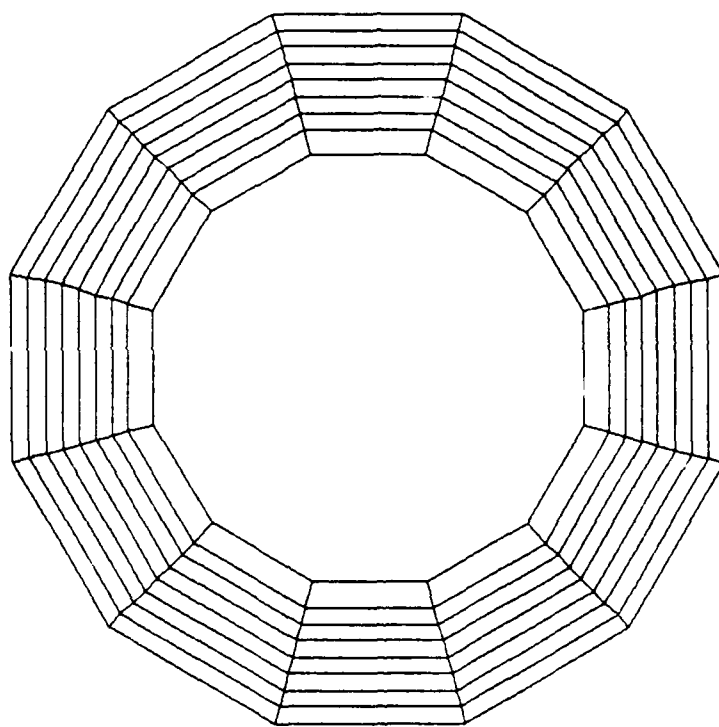


Figure 14. Top View of JFTOT Model of 8x12x14 (Case 2).

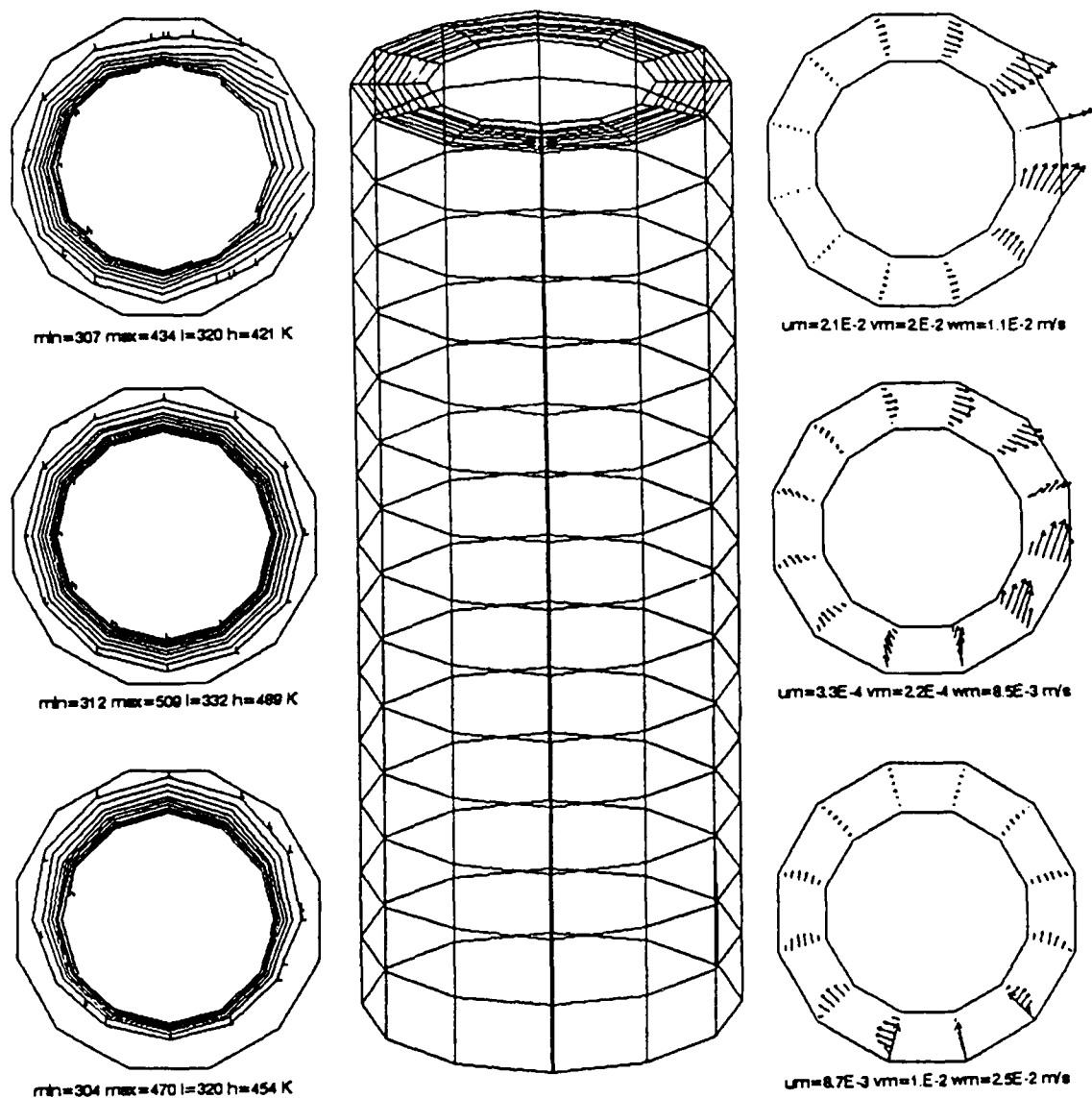


Figure 15. Calculated Temperature Contours and Velocity Vectors at the Bottom, Mid-Height, and Top of the FOM-JFTOT (Case 2, 2600 Cycles, Time = 4.1 Sec).

We see no significant differences among those three cases except the velocity vector profile at the mid-height. With more computational cells either in the azimuthal or in the axial coordinate, the radial and azimuthal velocities appear more dispersed or damped. For instance, the ratios of the axial velocity to the radial velocity at the mid-height are 241, 33, and 25 for the Base Case, Case 1, and Case 2, respectively. However, the thermal energy distributions are dominated by axial flow motions.

Figure 16 is comparable to Figures 7 and 11. Radial temperature and axial velocity profiles corresponding to the exit are nearly identical to those of Figures 7 and 11.

Figure 17 is the axial velocity profile azimuthally sliced at the inlet and the opposite side of the inlet, and the exit and the opposite side of the exit that can be compared to Figures 8 and 12. Figure 17 shows that the axial velocity at the inlet and exit for the reduced computational grid is nearly the same as those for a more refined grid, indicating that the computational grid of 8(radial)x12(azimuthal)x12(axial) is fairly good at simulating the JFTOT, thereby avoiding a lot of computer costs.

3.2 Sensitivity Study of Computing Time

The base case of 8 x 24 x 24 cells was run up to 3950 cycles to see if the temperature and velocity had reached a steady state. Figures 15 and 16 were velocity profiles of 3650 cycles, time = 5.8 seconds and 3950 cycles, time = 6.42 seconds at the mid-height. These are compared with the velocity vector profile at the mid-height shown in Figure 6.

As noted in Figures 6, 18, and 19, velocity vectors are more azimuthally oriented as time goes on. Also one can note an azimuthally oscillated flow pattern at the different computational time frame, indicating that azimuthal and radial velocities are still transient. However, the

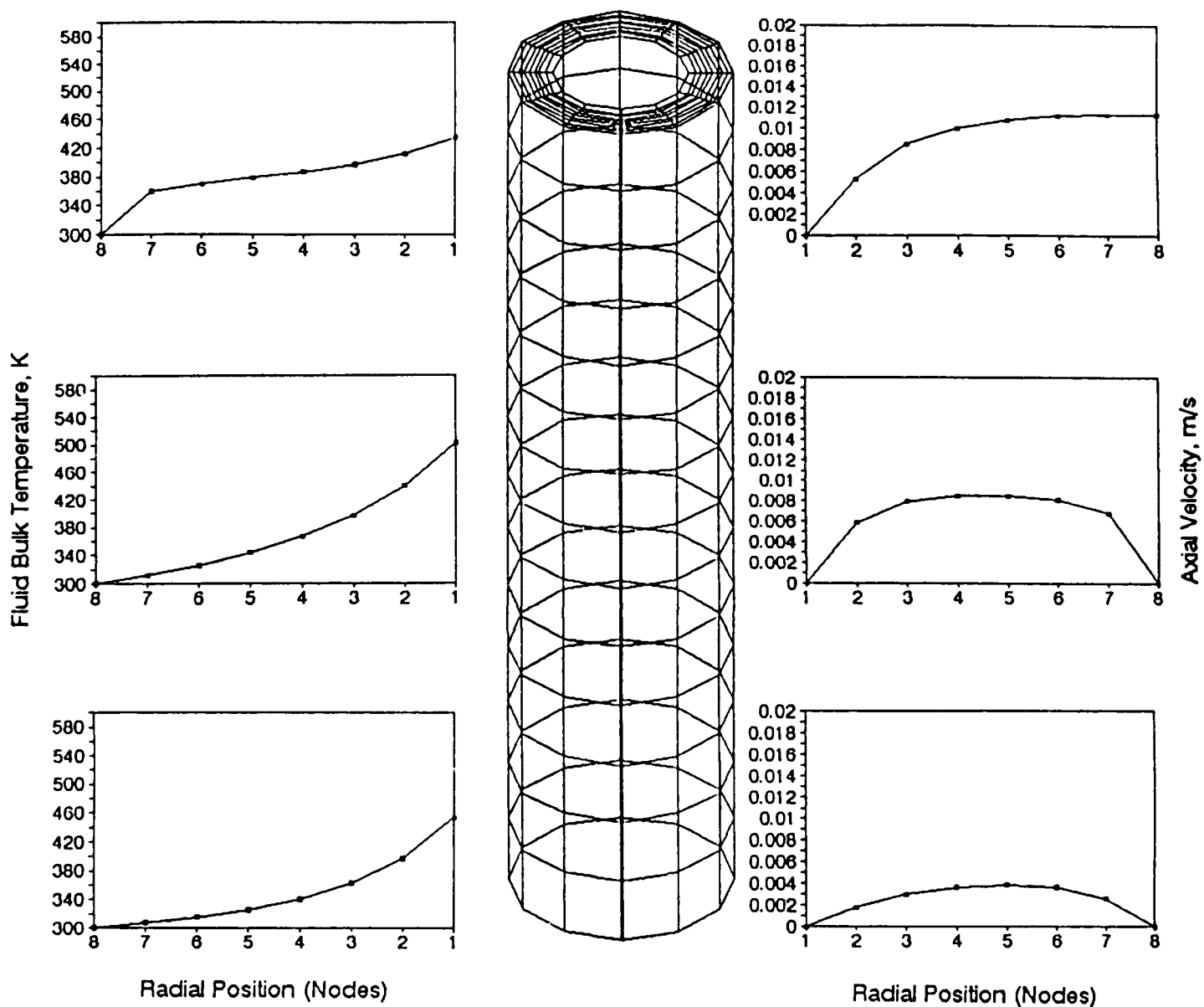


Figure 16. Calculated Radial Temperature and Velocity Distributions at the Bottom, Mid-Height, and Top of the FOM-JFTOT (Case 2).

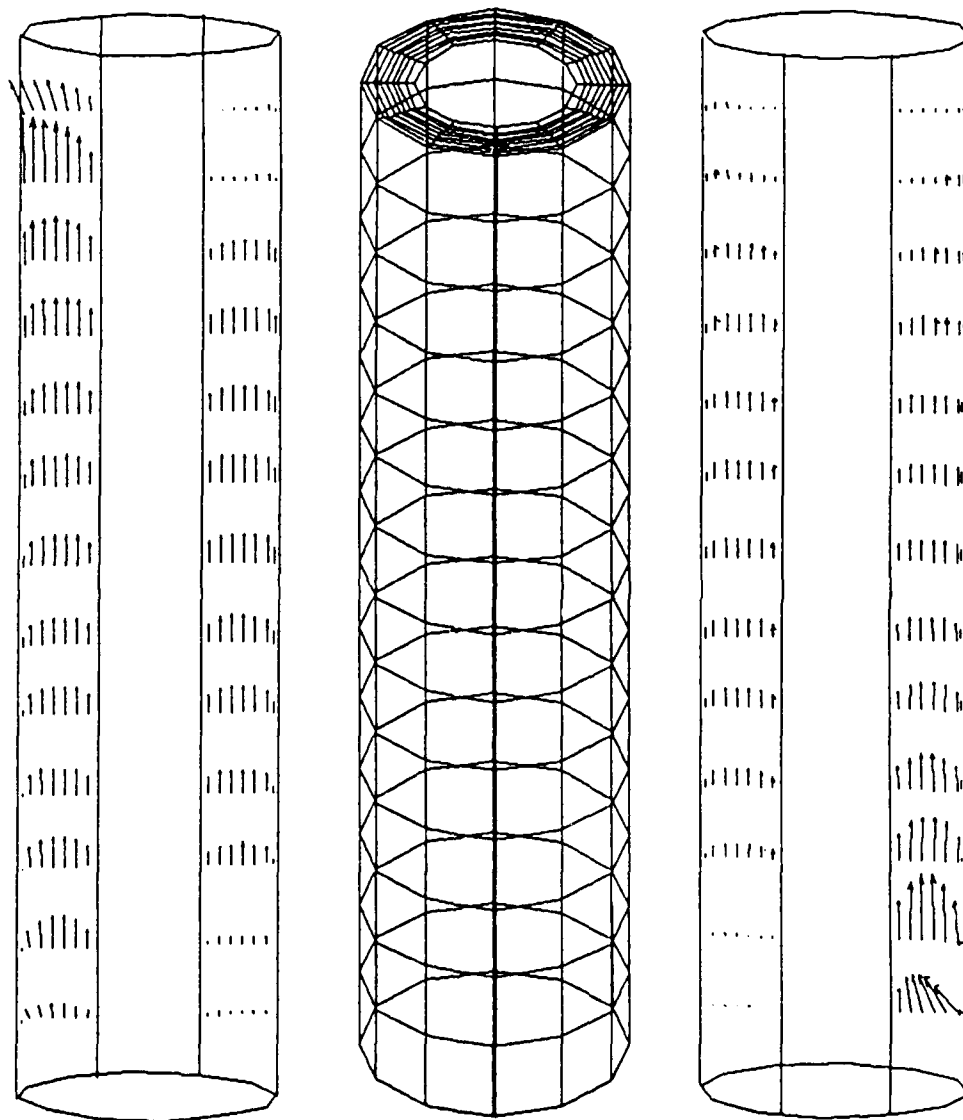
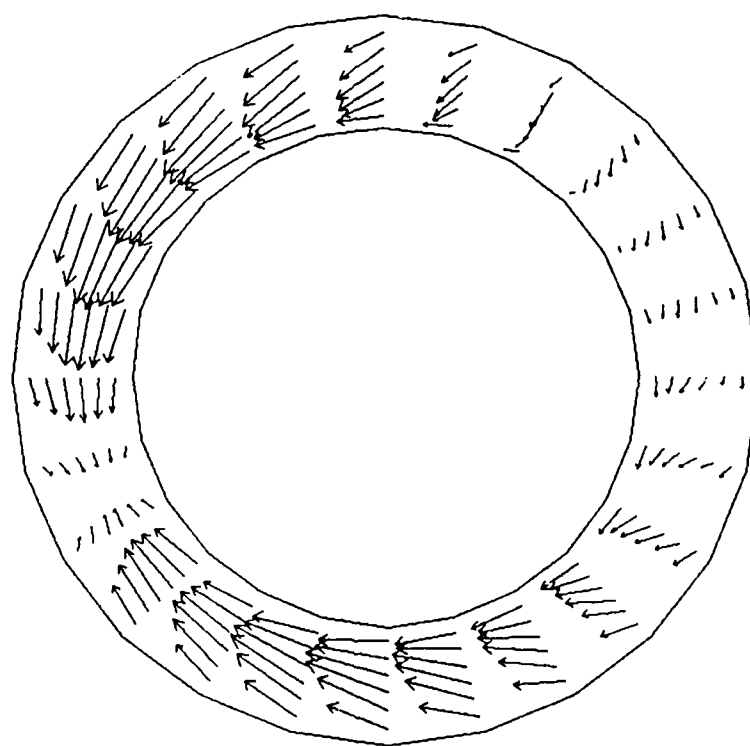
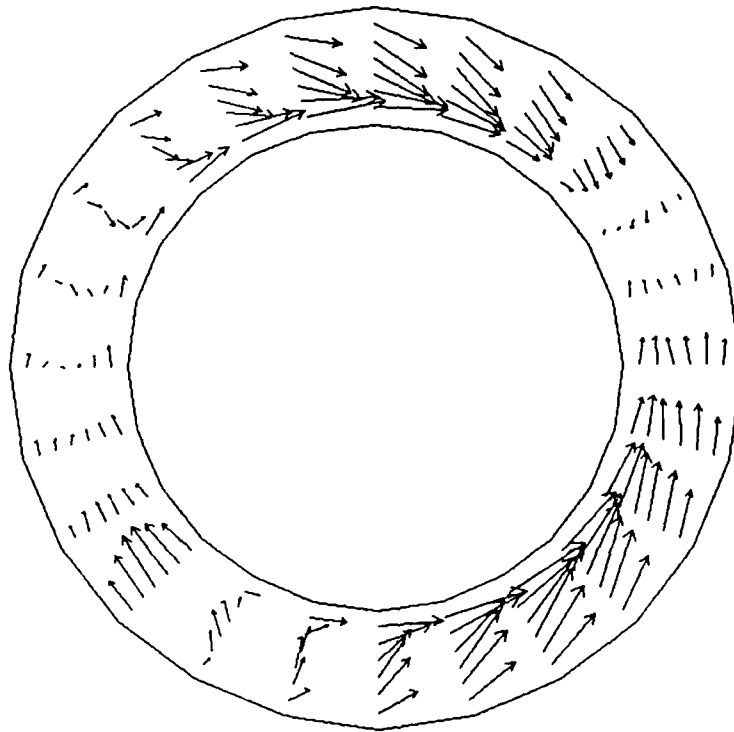


Figure 17. The Axial Velocity Vectors Corresponding to the Azimuthal Slices of the Inlet and Exit Plane (Case 2).



$u_m = 9.97451e-03$ $v_m = 9.18765e-03$ $w_m = 4.60424e-01$

Figure 18. Calculated Velocity Vectors at the Mid-Height for Sensitivity Study (Base Case, 3650 Cycles, Time = 5.8 Sec).



$u_m = 7.58489e-03$ $v_m = 5.43037e-03$ $w_m = 3.99318e-03$

Figure 19. Calculated Velocity Vectors at the Mid-Height for Sensitivity Study (Base Case, 3950 Cycles, Time = 6.42 Sec).

temperature contours are dominated by the axial velocity and Figures 20 and 21 indicate that temperatures appear to be at steady state.

3.3 Deposit Calculation

The inner aluminum tube surface temperature (eq. 29) was incorporated into KIVA, along with the physical property correlation of JP-5. The azimuthally uniform temperature and the interface temperature 300 K between the fluid and the inner housing were assumed. The system pressure and volumetric flow rate used in this computation were 3.45 MPa and 0.003 liter/min, respectively.

The rate of formation of deposit, dx/dt , is defined by the following equation as mentioned earlier in the Section IV (subsection 2).

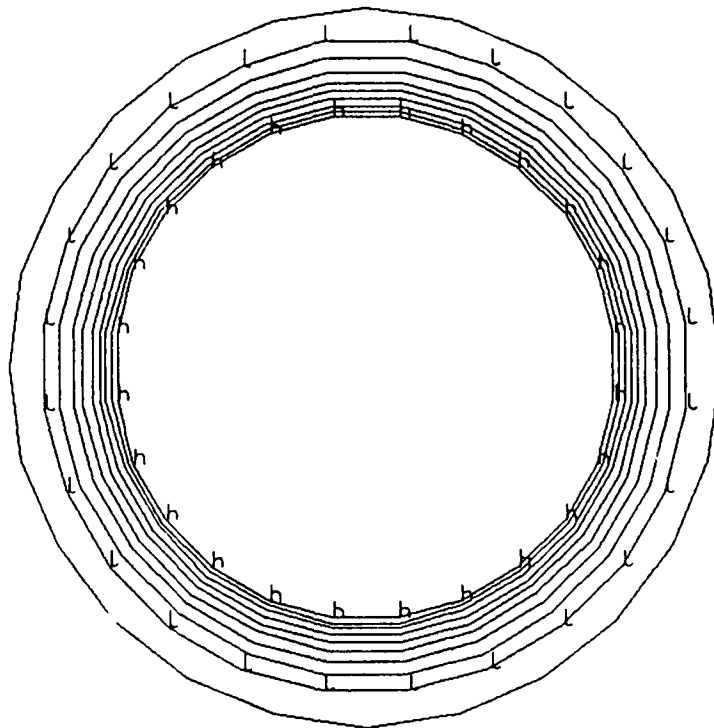
$$dx/dt = 155970 e^{(-19920/T)}, \text{ m/sec}$$

where T is the temperature of the tube wall expressed in degrees Kelvin.

Boundary heat flux and fluid temperatures obtained from KIVA were used as boundary conditions to calculate the azimuthal wall temperature and carbon deposit thickness by solving the following energy equation separately from KIVA in conjunction with the carbon deposition correlation above.

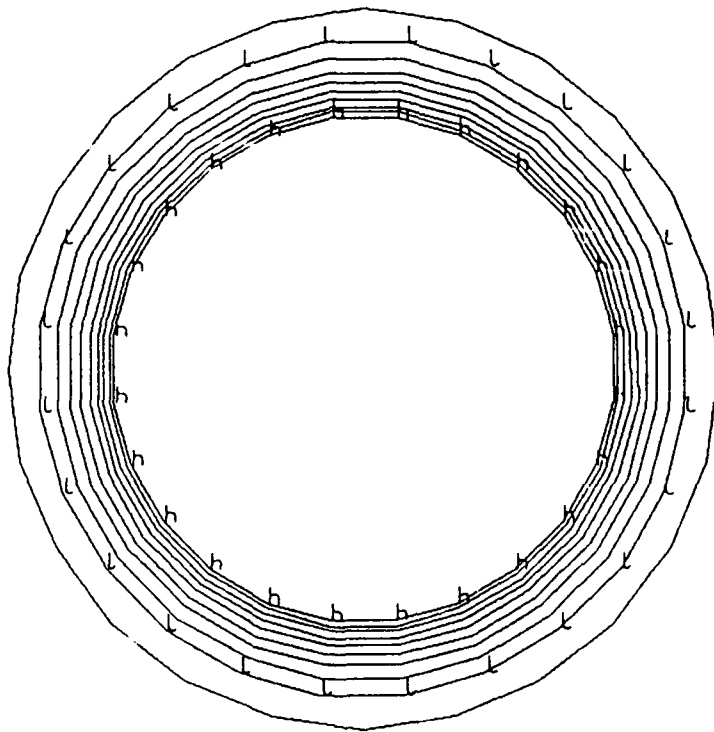
$$K \nabla^2 T = \left[\frac{1}{r} \frac{\partial}{\partial r} \left(K r \frac{\partial T}{\partial r} \right) + \frac{1}{r^2} \frac{\partial}{\partial \theta} \left(K \frac{\partial T}{\partial \theta} \right) \right] = 0 \quad (30)$$

Implicit in a deposition model such as this are a number of assumptions about the deposition process. First, it is assumed that the deposition depends on the temperature at the heater wall. It is also assumed



min= 3.11957E+02 max= 5.06272E+02 L= 3.31388E+02 h= 4.86840E+02

Figure 20. Calculated Temperature Contours at the
Mid-Height for Sensitivity Study
(Base Case, 3650 Cycles, Time = 5.8 Sec).



min= 3.12271E+02 max= 5.08577E+02 l= 3.31901E+02 h= 4.88946E+02

Figure 21. Calculated Temperature Contours at the Mid-Height
for Sensitivity Study (Base Case, 3950 Cycles,
Time = 6.42 Sec).

that the deposits accumulated at any position along a wall are due to the local wall temperature and are not affected by the transport mechanism in the vicinity of that particular location. Data to model the formation and transport of particles in the bulk do not exist, so global models have to suffice for initial studies.

Figure 22 shows axial profiles of the wall temperature and deposit thickness for the azimuthal location corresponding to the exit. The model being employed indicates that the growth of the deposit layer clearly follows the growth of the temperature along the tube. The maximum deposit thickness of 0.13 microns was calculated at 38 min at the hot spot where the wall temperature is 560 K, which compares favorably with the maximum measured deposit of 0.14 microns. Furthermore, the model is consistent with the experiment in predicting the location of the maximum deposit at the location of maximum tube temperature. However, the validity of this model is based on the very limited existing experimental data and assumptions made for the JFTOT boundary condition. This is primarily due to a lack of data of this nature. However, it is a start.

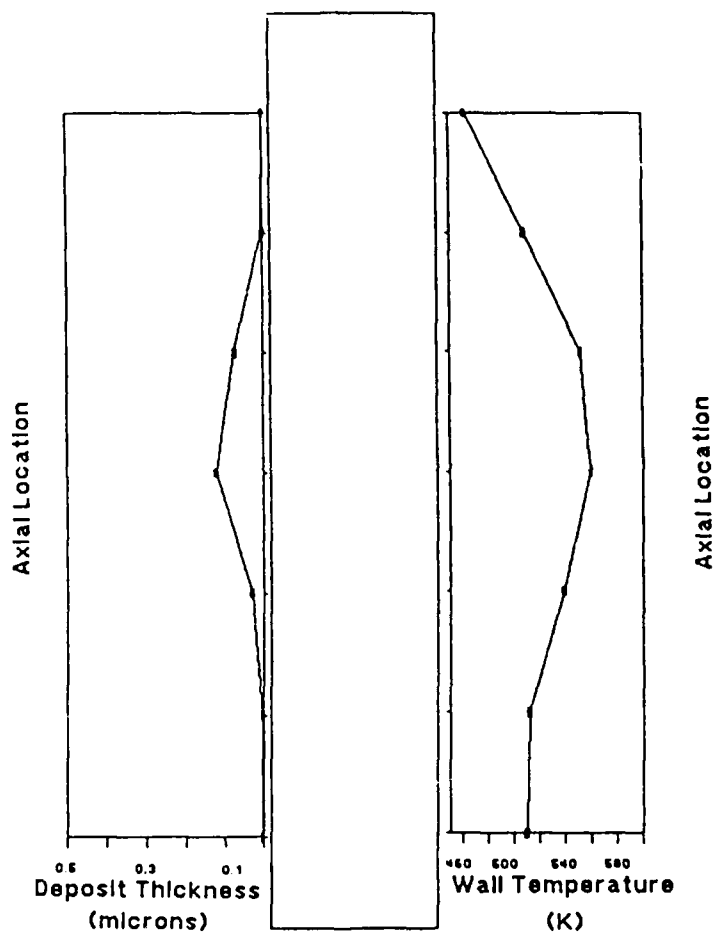


Figure 22. Calculated Deposit Thickness Profile on the FOM-JFTOT.

SECTION V

CONCLUSIONS AND RECOMMENDATIONS FOR FUTURE STUDIES

Temperature and velocity distributions in the FOM-JFTOT calculated from this study offer an aid in understanding fluid behavior that would eventually need to be coupled with the chemistry and heat transfer later in a future study. The CFDC model used in this study is based on the global Arrhenius type surface temperature-dependent correlation because of the lack of the existing experimental data. The initial attempt to simulate flow in the JFTOT is very encouraging. "Clean" experiments need to be done to define all the parameters pertinent to the deposition. The following are recommended for future studies.

1. Quantitative measurement of free oxygen and hydroperoxide radicals in the bulk stream as a function of temperature.
2. Accurate flow distribution measurement.
3. Measurement of JFTOT housing temperature (interface temperature between fluids and housing).
4. Qualitative data acquisition on particle removal from the deposit layer as a function of temperature and flow rate.
5. Qualitative (for instance, what chemical structure of sulfur) and quantitative impurity effect on deposition.

NOMENCLATURE

A_s	speed of sound in fluid
A_1	constant defined in eqn. 7
A_2	constant defined in eqn. 7
A	outward projected area
\bar{C}	concentration of fouling species
c	pH constant
E	activation energy defined in equation 7
f	friction factor
G	mass flux
I	internal energy
k	reaction rate constant
K	mass transfer coefficient
K	thermal conductivity defined in eqn. 30
M	cell face mass
N	mass flux
P	pressure
r	volume residual
R_f	fouling resistance
S	face-centered coupling coefficient
S_c	Schmidt number
t	time
T	temperature
u	velocity
U	velocity
V	volume
x	deposit thickness
X	axial distance defined in equation 29
\dot{X}	deposit rate defined in eqn. 7

GREEK

α	face number
θ	exposure time
γ	compressibility
λ	defined from $f = \lambda Re^{-0.2}$
μ	viscosity
π_1	defined in eqn. 10
π_2	defined in eqn. 11
ρ	density
τ	wall shear stress
ϕ	variable implicitness parameter
ψ	function of deposit structure

SUPERSCRIPT

A phase
B phase

SUBSCRIPT

b bulk
B bottom faces of cell ijk
D derriere faces of cell ijk
f foulant
f_b foulant at bulk
f_i foulant at interface
F front faces of cell ijk
i fluid-deposit interface
L left faces of cell ijk
m mixture
o referenced state
p precursor
Pb precursor at bulk
pi precursor at interface
R right faces of cell ijk
T top faces of cell ijk
w wall

SECTION VI

REFERENCES

1. P. A. Warner and T. B. Biddle, "Properties of Aircraft Fuels and Related Materials," FR 19032-11, United Technologies Corporation (1988).
2. A. A. Amsden, J. D. Ramshaw, P. J. O'Rourke, and J. K. Dukowicz, "KIVA: A Computer Program for Two- and Three-Dimensional Fluid Flows with Chemical Reactions and Fuel Sprays," LA-10245-MS, Los Alamos National Laboratory, (1985).
3. Creare Inc., "Fluent Solving Complex Problems in Fluid Dynamics," Mechanical Engineering, 21, (1986).
4. Fluid Dynamics International, "FIDAP General Introduction Manual," (1984).
5. B. Hutchings and R. Iannuzzell, "Taking the Measure of Fluid Dynamics", Mechanical Engineering (1987).
6. A. A. Amsden, J. D. Ramshaw, L. D. Cloutman, and P. J. O'Rourke, "Improvements and Extensions to the KIVA Computer Program," LA-10534-MS, Los Alamos National Laboratory, (1985).
7. P. J. O'Rourke and A. A. Amsden, "Implementation of a Conjugate Residual Iteration in the KIVA Computer Program," LA-10849-MS, Los Alamos National Laboratory (1986).
8. A. A. Amsden, P. J. O'Rourke, and T. D. Butler, "KIVA-II: A Computer Program for Chemically Reactive Flows with Sprays," LA-11560-MS, Los Alamos National Laboratory, (1989).
9. R. Bradley, R. Bankhead, and W. Bucher, "High Temperature Hydrocarbon Fuels Research in an Advanced Aircraft Fuel System Simulator on Fuel AFFB-14-70," AFAPL-TR-73-95 (1973).
10. A. Vranos and P. J. Marteney, "Experimental Study of the Stability of Aircraft Fuels at Elevated Temperatures," NASA CR-165165, United Technologies Research Center, (1980).
11. J. A. TeVelde and M. R. Glickstein, "Heat Transfer and Thermal Stability of Alternative Aircraft Fuels Vol. 1," NAPC-PE-87C, United Technology Pratt & Whitney, (1983).
12. J. A. TeVelde and M. R. Glickstein, "Heat Transfer and Thermal Stability of Alternative Aircraft Fuels Vol. 2," NAPC-PE-87C, United Technology Pratt & Whitney, (1983).
13. W. J. Purvis, "Investigation of Thermal Coking Rates of Air Force Jet Fuels," AFWAL-TR-84-2004, Wright-Patterson AFB, (1984).
14. C. R. Martel, "Military Jet Fuels," AFWAL-TR-87-2062, Wright-Patterson AFB, (1987).

15. ASTM D3241-73T, "Tentative Methods of Test for Thermal Oxidation Stability of Turbine Fuel," (JFTOT Procedure).
16. Coordinating Research Council, "CRC Literature Survey on the Thermal Oxidation Stability of Jet Fuel," CRC Report No. 509, (1979).
17. B. J. Reitzer, "Rate of Scale Formation in Tubular Heat Exchangers," Industrial and Engineering Chemistry Process Design and Development, Vol. 3, No. 4, (1964).
18. J. Taborek, T. Aoki, R. B. Ritter, and J. W. Palen, "Fouling: The Major Unresolved Problem in Heat Transfer," Chemical Engineering Progress, Vol 68, No. 2, (1972).
19. M. P. Bond, "Plate Heat Exchangers for Effective Heat Transfer," The Chemical Engineer, April (1981).
20. J. G. Knudsen and B. V. Roy, "Influence of Fouling on Heat Transfer," Proceedings of the Seventh International Heat Transfer Conference, Vol. 1, (1982).
21. P. J. Fryer, P. J. Hobin, and J. P. Mawer, "Optimal Design of a Heat Exchanger Undergoing Reaction Fouling," The Canadian Journal of Chemical Engineering, Vol. 66, (1988).
22. A. P. Watkinson and N. Epstein, "Particulate Fouling of Sensible Heat Exchangers," Proceedings of the 4th International Heat Transfer Conference, Paris, Vol. 1, (1970).
23. J. D. Smith, "Effects of Deposits on Heat Transfer to Aviation Kerosine," Industrial and Engineering Chemistry Process Design and Development, Vol. 8, No. 3, (1969).
24. R. E. Morris, R. N. Hazlett, and C. L. McIlvaine III, "The Effects of Stabilizer Additives on the Thermal Stability of Jet Fuel," Industrial and Engineering Chemistry Research, Vol. 27, No. 8, (1988).
25. J. C. Griess, H. C. Savage, and J. L. English, "Effect of Heat Flux on the Corrosion of Aluminum by Water, Part IV. Tests Relative to the Advanced Test Reactor and Correlation with Previous Results," ORNL-3541, Oak Ridge National Laboratory, (1964).
26. H. Muller-Steinhagen, F. Reif, N. Epstein, and A. P. Watkinson, "Influence of Operating Conditions on Particulate Fouling," The Canadian Journal of Chemical Engineering, Vol. 66, (1988).
27. J. W. Cleaver and B. Yates, "The Effect of Re-entrainment on Particle Deposition," Chemical Engineering Science, Vol. 31, (1976).
28. B. D. Crittenden, S. A. Hout, and N. J. Alderman, "Model Experiments of Chemical Reaction Fouling," Chemical Engineering Research and Design, Vol. 65, (1987).

29. R. N. Hazlett, J. M. Hall, and M. Matson, "Reactions of Aerated N-Dodecane Liquid Flowing Over Heated Metal Tubes," Industrial and Engineering Chemistry Production Design and Development, Vol. 16, No. 2, (1977).
30. M. Bajus, V. Vesely, P. A. Leciereq, and J. A. Rijks, "Steam Cracking of Hydrocarbons 2. Pyrolysis of Methycyclohexane," Industrial and Engineering Chemistry Production Research and Development, Vol. 18, No. 2, (1979).
31. F. R. Mayo, L. L. Stravinoha, and G. H. Lee, "Source of Jet Fuel Thermal Oxidation Tester Deposits from an Oxidized JP-8 Fuel," Industrial and Engineering Chemistry Research, Vol. 27, No. 2, (1988).
32. P. J. Marteney and L. J. Spadaccini, "Thermal Decomposition of Aircraft Fuel," Journal of Engineering for Gas Turbines and Power, Vol. 108, (1986).
33. W. F. Taylor, "Deposit Formation from Deoxygenated Hydrocarbons in General Features," Industrial and Engineering Chemistry Production Research and Development, Vol. 13, No. 2, (1974).
34. K. M. Sundaram, and G. F. Froment, "Comparison of Simulation Models for Empty Tubular Reactors," Chemical Engineering Science, 34, (1979).
35. J. Chen and M. J. Maddock, "How Much Spare Heater for Ethylene Plants?," Hydrocarb Process, 52, (5) (1973).
36. D. Q. Kern and R. E. Seaton, "A Theoretical Analysis of Thermal Surface Fouling," British Chemical Engineering, 4, (1959).
37. B. D. Crittenden, S. T. Kolaczowski, and S. A. Hout, "Modeling Hydrocarbon Fouling," Chemical Engineering Research and Design, Vol 65, (1987).

APPENDIX A
DIMENSION TABLES FOR JFTOT MODEL

Table A-1. Axial Dimension of 8x24x24 Cells

	<u>Axial Distance (m)</u>
K = 1	0.0000e-3
K = 2	1.0138e-3
K = 3	2.0276e-3
K = 4	4.8249e-3
K = 5	7.6221e-3
K = 6	1.04194e-2
K = 7	1.32166e-2
K = 8	1.60139e-2
K = 9	1.88111e-2
K = 10	2.16084e-2
K = 11	2.44056e-2
K = 12	2.72028e-2
K = 13	3.00000e-2
K = 14	3.27973e-2
K = 15	3.55945e-2
K = 16	3.83918e-2
K = 17	4.11890e-2
K = 18	4.39863e-2
K = 19	4.67835e-2
K = 20	4.95808e-2
K = 21	5.23780e-2
K = 22	5.51753e-2
K = 23	5.79725e-2
K = 24	5.89862e-2
K = 25	6.00000e-2

Table A-2. Axial Dimension of 8x24x14 Cells

	<u>Axial Distance (m)</u>
K = 1	0.0000e-3
K = 2	1.0138e-3
K = 3	2.0276e-3
K = 4	7.6221e-3
K = 5	1.32166e-2
K = 6	1.88111e-2
K = 7	2.44056e-2
K = 8	2.00000e-2
K = 9	3.55945e-2
K = 10	4.11890e-2
K = 11	4.67835e-2
K = 12	5.23780e-2
K = 13	4.79725e-2
K = 14	5.89862e-2
K = 15	6.00000e-2

K = 1, 2, and 3 open for inlet
K = 13, 14, and 15 open for exit.

Table A-3. Radial Dimension of JFTOT Model

	<u>Radial Distance (m)</u>
i = 1	1.4000e-3
i = 2	1.5625e-3
i = 3	1.6696e-3
i = 4	1.7768e-3
i = 5	1.8839e-3
i = 6	1.9911e-3
i = 7	2.0982e-3
i = 8	2.2054e-3
i = 9	2.3125e-3

i = 1 is the centerline of the heater rod thickness for the inner boundary.
Computational grid for fluid is from i = 2 to i = 9.

Table A-4. Azimuthal Dimension of JFTOT Model

For 12 cells, 0.5236 radians

j = 2, 3, and 4 for inlet

j = 5, 6, and 7 for exit.

For 24 cells, 0.2618 radians

j = 3, 4, 5, 6, and 7 for inlet

j = 9, 10, 11, 12, and 13 for exit.

APPENDIX B

PROGRAM LISTING FOR DEPOSIT LAYER CALCULATION

```

program cfilm
c
c   This is carbon thickness calculation for the final report.
c
c   the unit is in S.I.
c   heat flux = w/sq.m, thermal conductivity = w/m-K .
c   temperature = K, heat transfer coefficient = w/sq.m-K . c
   tkiva = fluid bulk temperature next to the wall, K.
c   hkiva = convective heat transfer coefficient, w/m*m-K. c
   condcl = thermal conductivity of carbon deposit, w/m-K. c
   condhr = thermal conductivity of the wall, w/m-K.
c   qkiva = average heat flux calculated from KIVA, w/m*m. c
   acon = pre-exponential constant.
c   bcon = exponential constant.
   implicit real*8(a-h,o-z)
   dimension t(5,24),condi(5,24),condj(5,24),aw(5,24),ae(5,24)
   ..      an(5,24),as(5,24),ap(5,24),hkiva(24),qbc(24)
   ..      rad(5),tkiva(24),r(5,24),fthk(24),qgrad(5,24)      data
condcl / 0.121/
data condhr / 18.83/
data omega / 1.5 /
c
c   k = 15
c
c   data tkiva / 506., 506., 506., 506., 506., 506.,
+               506., 506., 506., 506., 506., 506.,
+               507., 507., 507., 507., 507., 507.,
+               507., 507., 506., 506., 506., 506. /
data hkiva / 12852., 12852., 12852., 12852., 12852., 12852.,
+           12852., 12852., 12852., 12852., 12852., 12852.,
+           13094., 13094., 13094., 13094., 13094., 13094.,
+           13094., 13094., 12852., 12852., 12852., 12852.
/
data qkiva / 6.94e5/
data acon / 1.5597e5/
data bcon / 19920./
data timend / 2250./
data dt / 60.0 /
data rad / 0.001150, 0.00135625, 0.0015625,0.,0./
c
open(6,file='cfilm.out',status='unknown')
dthko = 1.e-6
rad(4) = rad(3) + dthko
rad(5) = rad(4) + dthko
delth = 2.*3.14159/24
qkiva = qkiva*rad(5)/rad(1)
c
c * * * form conductance matrix
c
do 10 i = 1,5
do 10 j = 1,24
r(i,j) = rad(i)
condi(i,j) = condhr
if(i.eq.4) condi(i,j) = condcl
if(i.eq.5) condi(i,j) = hkiva(j)*(rad(i) - rad(i-1))

```



```

10 continue
c
do 20 i = 1,5
do 20 j = 1,24
condj(i,j) = condhr
if(i .eq. 4) condj(i,j) = condcl
if(i.eq.5) conej(i,j) = condcl
20 continue
c
do 30 i = 1,5
do 30 j = 1,24
t(i,j) = tkiva(j)
30 continue
c
100 time = time + dt
c
do 110 j = 1,24
c
temp = 561 K case
c
r(4,j) = r(4,j) + dt*acon*exp(-bcon/t(4,j))
r(5,j) = r(4,j) + dthko
110 continue
c
do 120 i = 1,4
do 120 j = 1,24
im = i-1
if(im.eq.0) im = 1
ip = i + 1
rp = 0.5*(r(ip,j)+r(i,j))
rm = 0.5*(r(im,j)+r(i,j))
drp = amax1((r(ip,j) - r(i,j)),dthko)
drm = amax1((r(i,j) - r(im,j)),dthko)
dr = rp - rm
an(i,j) = condj(i,j)/(r(i,j)*delth)**2
as(i,j) = an(i,j)
ae(i,j) = condi(ip,j)*rp/(r(i,j)*drp*dr)
if(i.eq.1) then
aw(i,j) = 0.0
qbc(j) = rm*qkiva/(dr*r(i,j))
else
aw(i,j) = condi(i,j)*rm/(r(i,j)*drm*dr)
endif
ap(i,j) = aw(i,j)+ae(i,j)+as(i,j)+an(i,j)
120 continue
c
nloop = 0
1000 nloop = nloop + 1
deltmx = 0.0
c
do 130 i = 1,4
do 130 j = 1,24
c
im = i-1

```

```

      if(i.eq.1) im = i
      ip = i+1
      jp = j+1
      if(j.eq.24) jp = 1
      jm = j-1
      if(j.eq.1 ) jm = 24
      flg = 0.0
      if(i.eq.1) flg = 1.0
      tsave = t(i,j)
      t(i,j) = (aw(i,j)*t(im,j)+ae(i,j)*t(ip,j)+an(i,j)*t(i,jp)
      .      +as(i,j)*t(i,jm)+flg*qbc(j))/ap(i,j)
      t(i,j) = tsave + omega*(t(i,j) - tsave)
      delt = abs(t(i,j) - tsave)
      if(t(i,j).ne.0.0) delt = delt/t(i,j)
      deltmx = amax1(deltmx,delt)
130  continue
      if(deltmx.gt.5.e-6 .and. nloop.lt.20000) go to 1000
c
      if(amod(time,60.*10.) .ne. 0. .and.
      .      time .lt. timend
      .      ) go to 160
      do 135 i = 1,4
      do 135 j = 1,24
      ip = i+1
      grad(i,j) = -condi(ip,j)*(t(ip,j)-t(i,j))/(r(ip,j)-r(i,j))
135  continue
c
      timem = time/(60.)
      write(6,*) 'time(min)=',timem
      do 140 j = 1,24
      write(6,*) 'j=',j
      write(6,146) (t(i,j), i=1,5)
      write(6,147) (grad(i,j), i=1,4)
140  continue
145  format(5(1x,1pelli.4))
146  format(' T =',5(1x,1pelli.4))
147  format(' qr=',5(1x,1pelli.4))
      do 150 j = 1,24
      fthk(j) = r(4,j) - r(3,j) - dthko
150  continue
      write(6,*) ' carbon film thickness'
      write(6,145) (fthk(j), j=1,24)
c
160  if(time.lt.timend) go to 100
c
      stop
      end

```

APPENDIX C
ENLARGED FIGURES

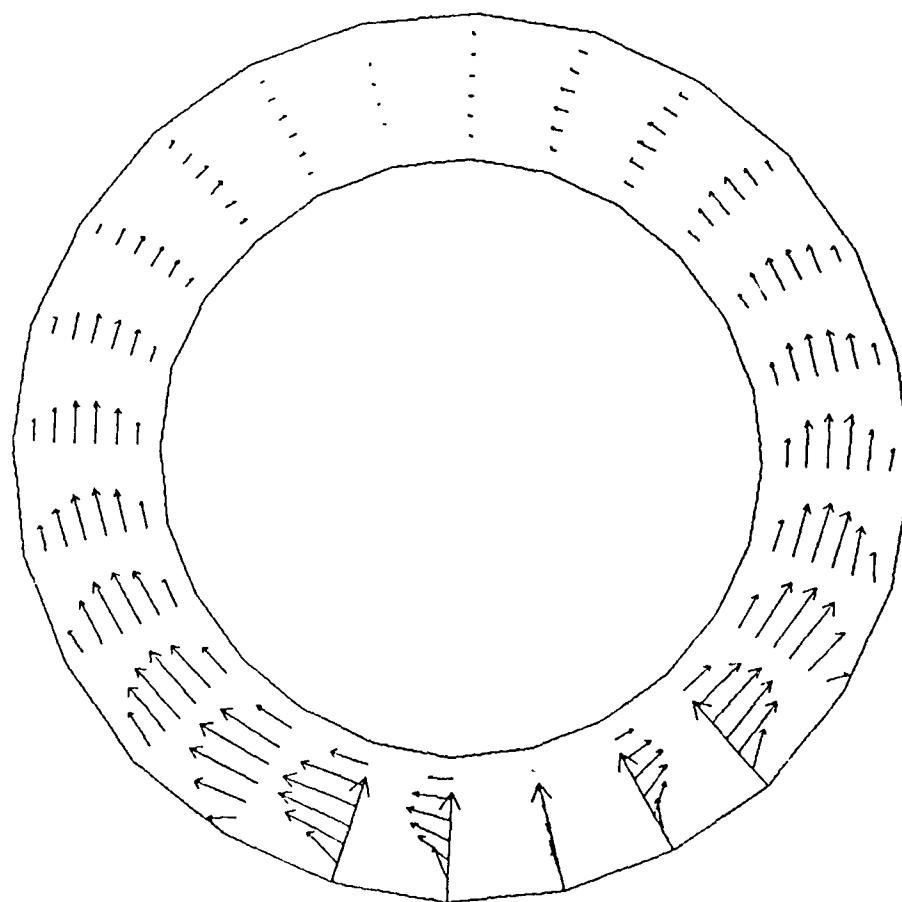


Figure C-1. Enlarged Velocity Vectors (Bottom) of Figure 6.

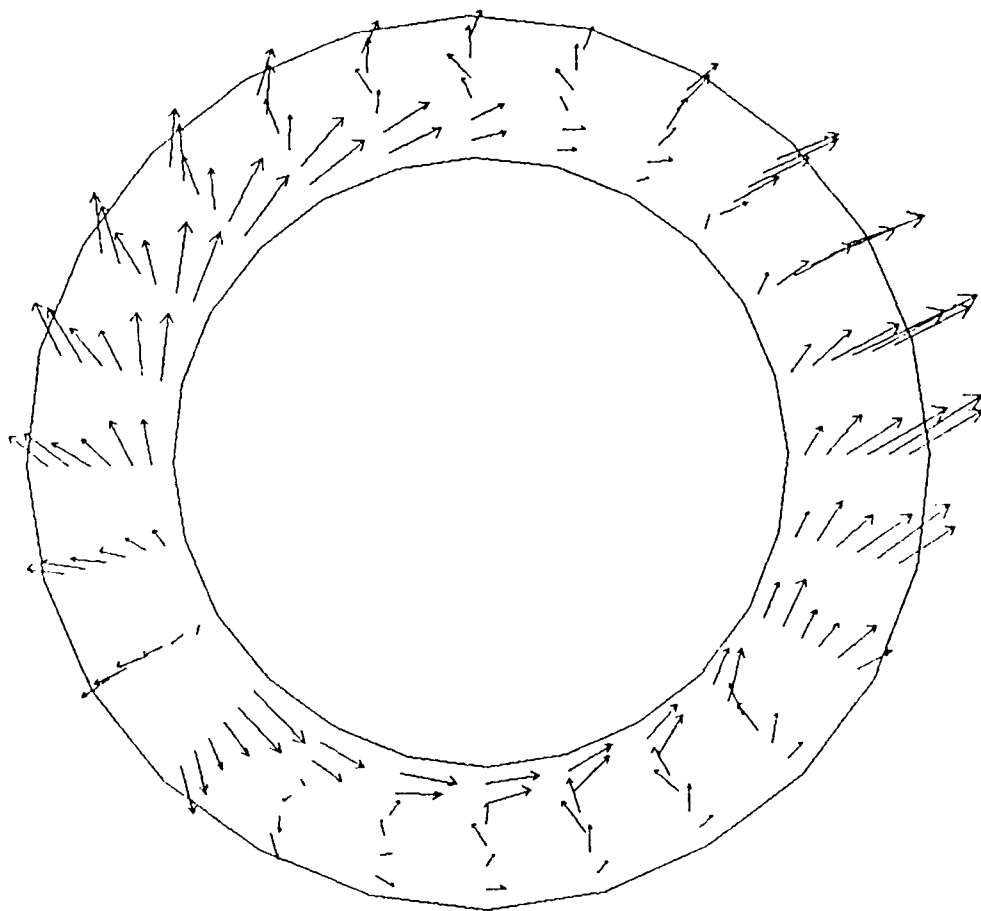


Figure C-2. Enlarged Velocity Vectors (Mid-Height) of Figure 6.

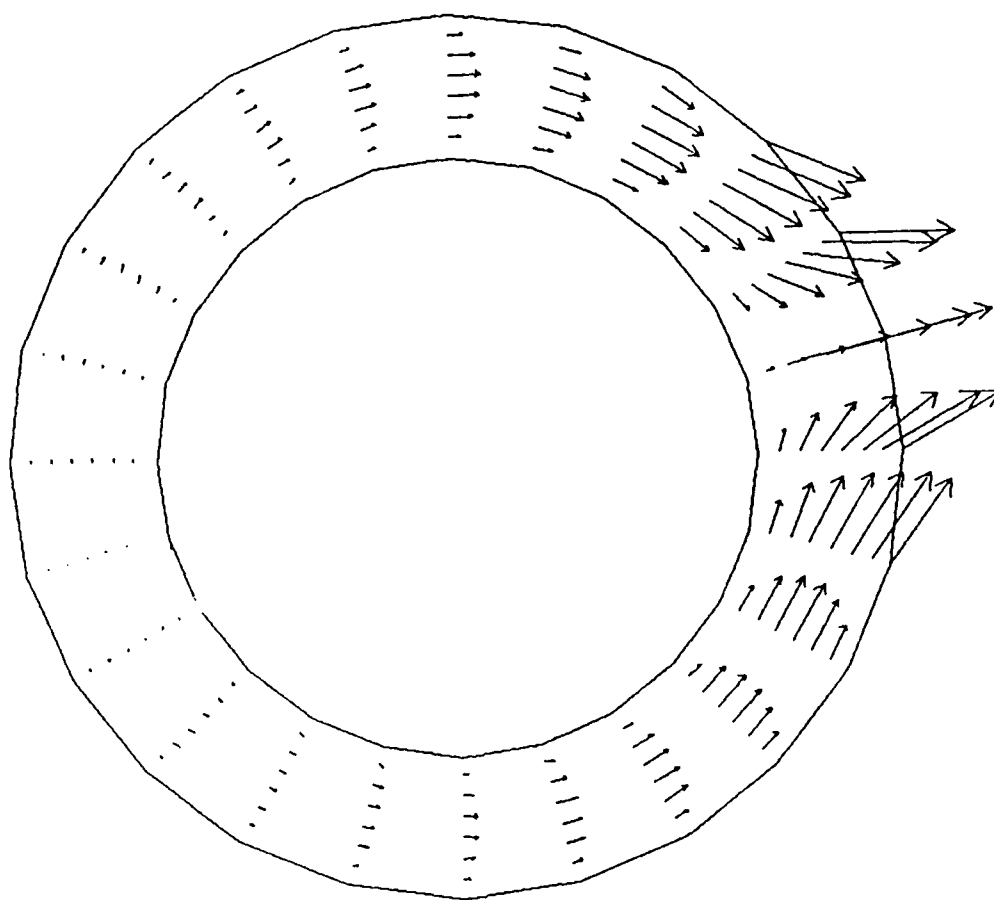


Figure C-3. Enlarged Velocity Vector (Top) of Figure 6.